

This document is downloaded from DR-NTU, Nanyang Technological University Library, Singapore.

Title	The 2010 Mw 7.8 Mentawai earthquake : very shallow source of a rare tsunami earthquake determined from tsunami field survey and near-field GPS data.
Author(s)	Hill, Emma M.; Borrero, Jose C.; Huang, Zhenhua.; Qiu, Qiang.; Banerjee, Paramesh.; Natawidjaja, Danny H.; Elosegui, Pedro.; Fritz, Hermann M.; Suwargadi, Bambang W.; Pranantyo, Ignatius Ryan.; Li, LinLin.; Macpherson, Kenneth A.; Skanavis, Vassilis.; Synolakis, Costas E.; Sieh, Kerry.
Citation	Hill, E. M., Borrero, J. C., Huang, Z., Qiu, Q., Banerjee, P., Natawidjaja, D. H., et al. (2012). The 2010 Mw 7.8 Mentawai earthquake : very shallow source of a rare tsunami earthquake determined from tsunami field survey and near-field GPS data. Journal of Geophysical Research, 117.
Date	2012
URL	<a href="http://hdl.handle.net/10220/8666">http://hdl.handle.net/10220/8666</a>
Rights	© 2012 the American Geophysical Union. This paper was published in Journal of Geophysical Research and is made available as an electronic reprint (preprint) with permission of the American Geophysical Union. The paper can be found at the following official DOI: <a href="http://dx.doi.org/10.1029/2012JB009159">http://dx.doi.org/10.1029/2012JB009159</a> . One print or electronic copy may be made for personal use only. Systematic or multiple reproduction, distribution to multiple locations via electronic or other means, duplication of any material in this paper for a fee or for commercial purposes, or modification of the content of the paper is prohibited and is subject to penalties under law.

## The 2010 $M_w$ 7.8 Mentawai earthquake: Very shallow source of a rare tsunami earthquake determined from tsunami field survey and near-field GPS data

Emma M. Hill,<sup>1</sup> Jose C. Borrero,<sup>2,3</sup> Zhenhua Huang,<sup>1,4</sup> Qiang Qiu,<sup>1</sup> Paramesh Banerjee,<sup>1</sup> Danny H. Natawidjaja,<sup>5</sup> Pedro Elosegui,<sup>6</sup> Hermann M. Fritz,<sup>7</sup> Bambang W. Suwargadi,<sup>5</sup> Ignatius Ryan Pranantyo,<sup>8</sup> LinLin Li,<sup>1</sup> Kenneth A. Macpherson,<sup>1</sup> Vassilis Skanavis,<sup>9</sup> Costas E. Synolakis,<sup>3,10</sup> and Kerry Sieh<sup>1</sup>

Received 14 January 2012; revised 6 April 2012; accepted 15 April 2012; published 5 June 2012.

[1] The  $M_w$  7.8 October 2010 Mentawai, Indonesia, earthquake was a “tsunami earthquake,” a rare type of earthquake that generates a tsunami much larger than expected based on the seismic magnitude. It produced a locally devastating tsunami, with runup commonly in excess of 6 m. We examine this event using a combination of high-rate GPS data, from instruments located on the nearby islands, and a tsunami field survey. The GPS displacement time series are deficient in high-frequency energy, and show small coseismic displacements (<22 cm horizontal and <4 cm subsidence). The field survey shows that maximum tsunami runup was >16 m. Our modeling results show that the combination of the small GPS displacements and large tsunami can only be explained by high fault slip at very shallow depths, far from the islands and close to the oceanic trench. Inelastic uplift of trench sediments likely contributed to the size of the tsunami. Recent results for the 2011  $M_w$  9.0 Tohoko-Oki earthquake have also shown shallow fault slip, but the results from our study, which involves a smaller earthquake, provide much stronger constraints on how shallow the rupture can be, with the majority of slip for the Mentawai earthquake occurring at depths of <6 km. This result challenges the conventional wisdom that the shallow tips of subduction megathrusts are aseismic, and therefore raises important questions both about the mechanical properties of the shallow fault zone and the potential seismic and tsunami hazard of this shallow region.

**Citation:** Hill, E. M., et al. (2012), The 2010  $M_w$  7.8 Mentawai earthquake: Very shallow source of a rare tsunami earthquake determined from tsunami field survey and near-field GPS data, *J. Geophys. Res.*, 117, B06402, doi:10.1029/2012JB009159.

### 1. Introduction

[2] Scientific research is often an exercise in detective work, but the case of so-called “tsunami earthquakes” [Kanamori, 1972; Polet and Kanamori, 2000; Lay and Bilek,

2007; Okal and Newman, 2001] is particularly vexing. These rare events cause very large tsunamis relative to their seismic magnitude, and have long puzzled geoscientists, in part because only a handful have occurred within the time of modern seismic instrumentation. One example of such a mystery is the 2006 Java earthquake, which was followed by a tsunami with 21-m runup despite having a relatively moderate ( $M_w$  7.8) seismic magnitude [Fritz et al., 2007].

[3] The  $M_w$  7.8 Mentawai earthquake of 25 October 2010 was a tsunami earthquake. It occurred seaward of the southern Mentawai islands of Sumatra, Indonesia (Figure 1), and preceded a very large tsunami that caused substantial damage and 509 deaths [casualty information from Pusdalops PB Sumbar (the Disaster Management Operational Control Center for West Sumatra Province)]. Maximum measured tsunami runup was >16 m. Seismological solutions indicate a shallow dip, consistent with an origin on the Sunda megathrust.

[4] Sumatra presents an unusual opportunity for monitoring a subduction zone because it has a chain of islands between the mainland and the oceanic trench. Thus, land-based observations are possible quite close to the shallow, locked portions of the megathrust. The Sumatra GPS Array

<sup>1</sup>Earth Observatory of Singapore, Nanyang Technological University, Singapore.

<sup>2</sup>ASR Limited, Marine Consulting and Research, Raglan, New Zealand.

<sup>3</sup>University of Southern California, Los Angeles, California, USA.

<sup>4</sup>School of Civil and Environmental Engineering, Nanyang Technological University, Singapore.

<sup>5</sup>LIPi Geoteknologi, Bandung, Jawa, Indonesia.

<sup>6</sup>Institute for Space Sciences and Marine Technology Unit, CSIC, Barcelona, Spain.

<sup>7</sup>Georgia Institute of Technology, Savannah, Georgia, USA.

<sup>8</sup>Institut Teknologi Bandung, Bandung, Indonesia.

<sup>9</sup>Technical University of Crete, Chania, Greece.

<sup>10</sup>Hellenic Center for Marine Research, Anavyssos, Greece.

Corresponding author: E. M. Hill, Earth Observatory of Singapore, Nanyang Technological University, 50 Nanyang Ave., N2-01a-15, Singapore 639798. (ehill@ntu.edu.sg)

Copyright 2012 by the American Geophysical Union.  
0148-0227/12/2012JB009159

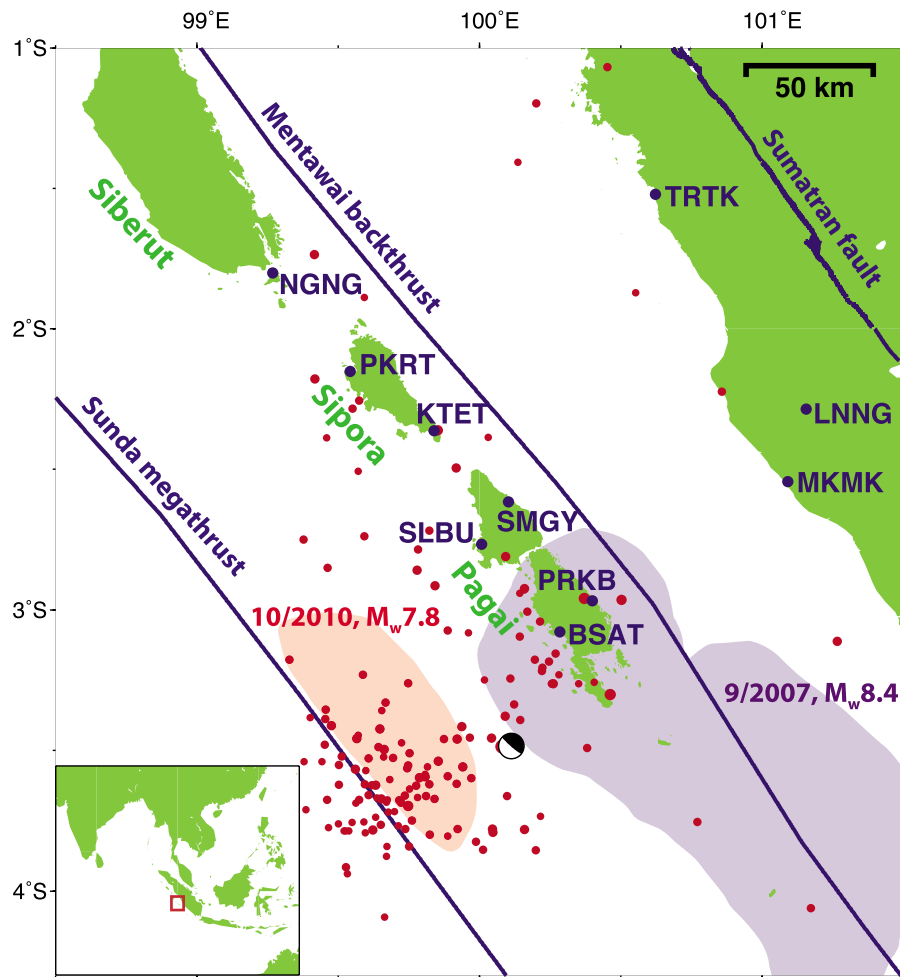


**Figure 1.** Location of the October 2010  $M_w$  7.8 Mentawai main shock (focal mechanism) and aftershocks (red dots). SuGAR GPS station locations are marked with blue dots. Approximate rupture patches for this earthquake ( $\sim 3.0$  m slip contour) and the September 2007  $M_w$  8.4 event [Konca *et al.*, 2008] are indicated in pink and purple, respectively. The inset map shows the regional location of our network, with the area of the larger map marked by the red rectangle. For both figures, land is colored green and oceans in white.

(SuGAR) spans the length of these islands and collected data, sampled once every second, through the time of the 2010 Mentawai earthquake. These dense, high-rate, and proximal data afford a very unusual opportunity to study both the static and kinematic rupture processes of a tsunami earthquake.

[5] That said, our modeling reveals a megathrust rupture so shallow and close to the trench that even our island-based monitoring stations were not close enough to observe the majority of the fault slip. This, therefore, is where the forensic work comes in. On the one hand, our post-tsunami field survey and modeling show how much displacement of the seafloor is required to produce the magnitude of the observed tsunami. On the other hand, relatively small GPS displacements on the islands show that high levels of slip on the megathrust cannot have occurred anywhere within tens of km of the islands. Modeling the combination of these two data sources leads us to the deduction that significant slip must have occurred in a very narrow and shallow strip near the trench.

[6] We first describe the tsunami data we collected from the island coasts soon after the tsunami, and displacement estimates derived from the high-rate GPS observations. Next, we describe plausible coseismic slip models obtained by combining these two sources of information. Since the size and destructive power of tsunamis are determined largely by the amplitude and area of vertical seafloor displacement, which, in turn, are determined by the amount of slip on the fault, we use the tsunami data to place a priori slip constraints on the GPS inversion for coseismic fault slip, producing a very different result from that obtained from GPS data alone.

## 2. Tsunami Data

[7] The tsunami field survey began on 10 November 2010, departing by ship from Bengkulu, Sumatra, and traveling through the Mentawai Islands (South and North Pagai, Sipora, and Southern Siberut) (Figure 1). The team visited 28 locations, measuring tsunami runup heights, flow depths,

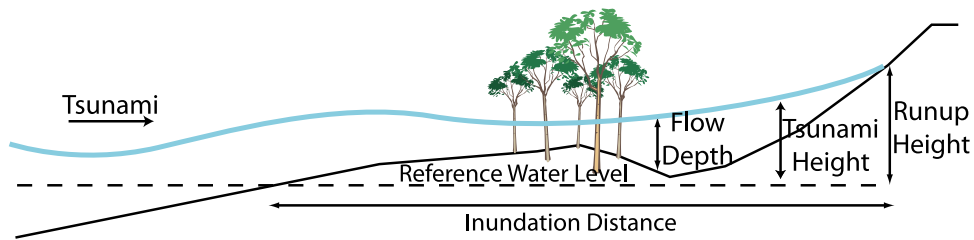


**Figure 2.** A schematic showing quantities measured in a post-tsunami field survey.

and inundation distances using standard techniques. In most locations, where the topography was flat and the surge extended deep into the forest, it was only possible to measure flow depths over ground rather than true runup heights (see Figure 2 for definitions of these terms). In addition to measuring physical parameters, the field team conducted interviews with eyewitnesses and local residents to obtain information on the timing and sequence of events, public response and evacuation, and the overall awareness of tsunami hazards in the various communities. Multiple photographs and videos were taken at each location, while witness interviews were recorded through note taking or on video.

[8] All runup and tsunami height measurements were corrected for tides by calculating the difference between the tide level at the time of the survey to the tide level at the time of the tsunami. Tide levels were determined using the method described in *Meltzner et al.* [2010], with the tide level 30 minutes after the earthquake used as the reference sea level. Because the tide range in the Mentawai Islands is not particularly large (approximately 1 m total range) the overall corrections were not substantial relative to the magnitude of the tsunami. The largest correction applied was

~0.4 m, which represents less than 10% of the total tsunami height at that location.

[9] Along the west coast of the Mentawai Islands, from southern Siberut to the southern tip of South Pagai Island, tsunami heights generally ranged from 1 to 10 m (Figure 3) with the strongest effects observed along the west coasts of North and South Pagai islands. Maximum tsunami heights were measured along the western shores of a string of small islands west of South Pagai. On one of these islands, Sibigau, we recorded a maximum runup of 16.9 m, with similar measurements of 12.6, 14.8 and 10.2 m recorded at locations nearby (Figure 3). It should be noted that these values are measurements of true runup height, i.e., the situation where the tsunami wave reaches a maximum elevation against topographical relief. Satellite imagery and photos taken during the survey (Figures 4 and 5) show the extent of the damage in this area. Two cross-shore profiles from Sibigau, each stretching approximately 600 m from the shoreline to the point of maximum runup are shown in Figure 6, along with flow depths inferred during the survey. Figure 6 also depicts transects measured across another nearby island, South Libaut, which suggest complete overtopping and

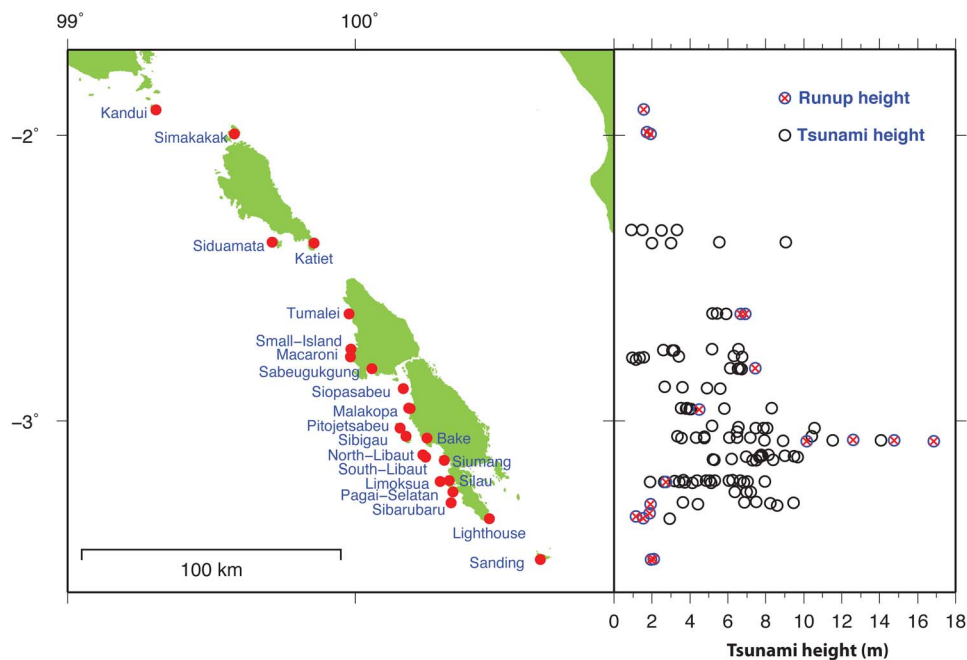


**Figure 3.** Water-level measurements along the west coast of the Mentawai Islands from the October 2010 tsunami. Measurements shown on the right side of the figure correspond in latitude to the locations shown on the left.

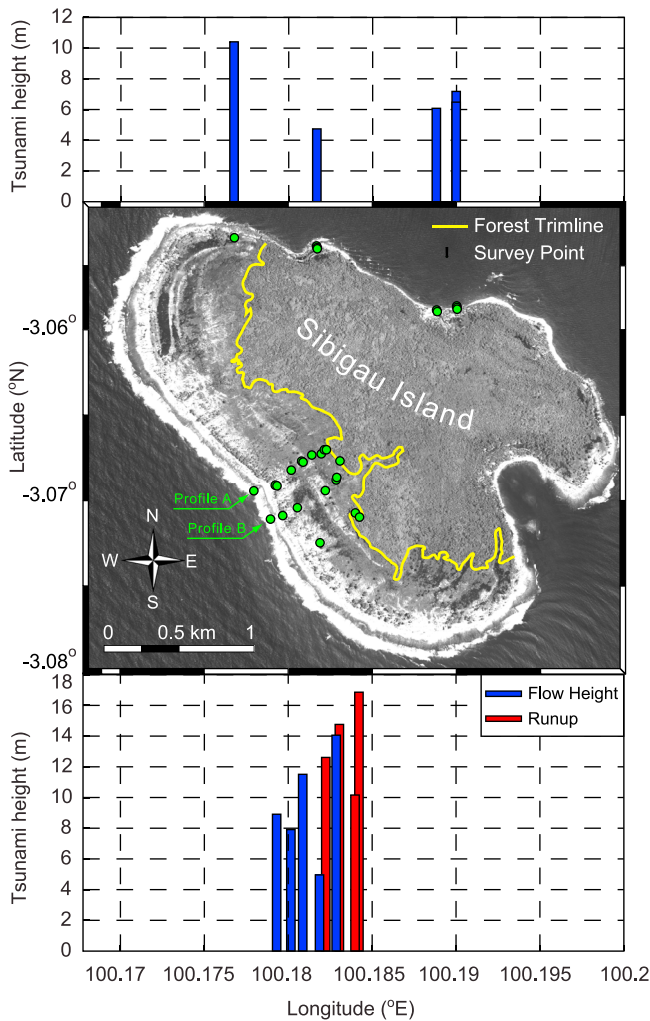


**Figure 4.** Sibigau Island: Measured tsunami and runup heights with survey point locations on post-tsunami satellite image (acquired 1 November 2010 by Worldview-1). The trimline of forest destruction is based on a comparison of pre- and post-event satellite imagery and matches the runup points.

temporary submergence of the entire island by the tsunami surge. Additional details can be found in the complete field survey report (Text S2 of the auxiliary material).<sup>1</sup>

[10] Based on information gathered from eyewitness interviews conducted during the survey, the earthquake was not strongly felt. Residents described it as a gentle, slow, rocking earthquake that lasted for several minutes. These accounts are consistent with seismological observations that this earthquake was deficient in high-frequency energy and had a long rupture time [Newman *et al.*, 2011; Lay *et al.*, 2011], a defining feature of tsunami earthquakes [Kanamori, 1972; Polet and Kanamori, 2000]. Witnesses to the earthquake and tsunami reported that the time interval between the earthquake and the first peak tsunami wave was between

<sup>1</sup>Auxiliary material data sets are available at <ftp://ftp.agu.org/apend/jb/2012/jb009159>. Other auxiliary material files are in the HTML. doi:10.1029/2012JB009159.

5 and 10 min, and that the tsunami comprised three main waves.

[11] One of the interviewees, Captain Lee Clarke, gave a particularly vivid account of the tsunami. His boat, the *M.V. Freedom III*, was anchored in Macaronis Bay (Figure 3) on the night of the earthquake. The captain stated that around 10:00 pm local time, shortly after going to bed, he got up for an unknown reason to check the boat's surroundings. He does not recall feeling an earthquake, but noted that one of the crewmen reported that he may have felt the earthquake. While conducting his check, the captain noticed that a strong current was pulling the vessel toward the entrance of the bay, indicating that the water level was dropping. (The fact that the water withdrew is suggestive of a leading depression N-wave.) Looking out over the stern of the vessel, he noticed a wave approaching as a bore front that he estimated to be 5 m in height. He also noted that the wave had broken at the entrance to the bay, where the water is on the order of 10 m deep.

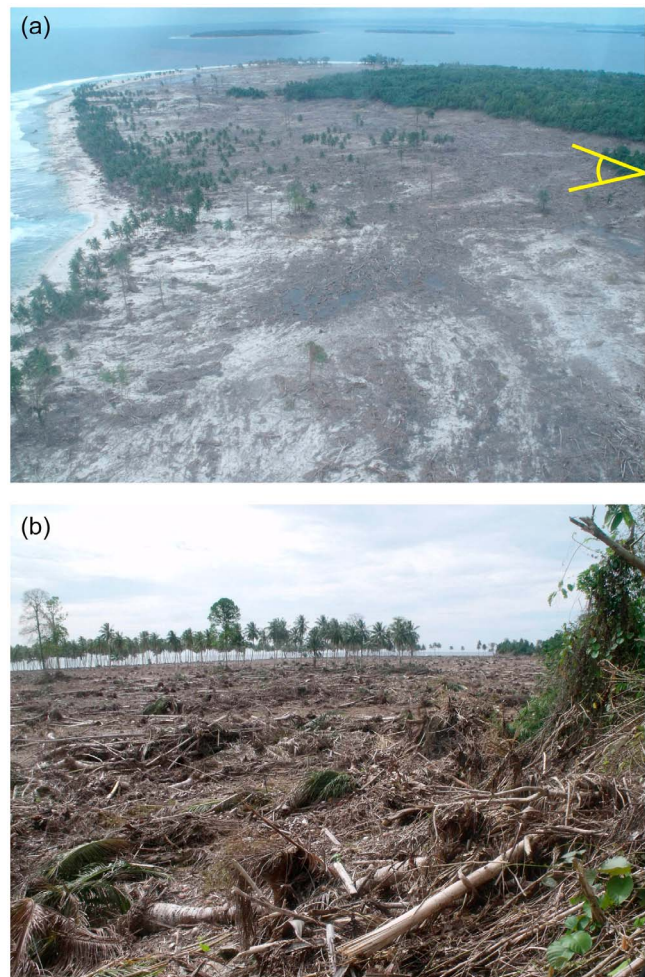


**Figure 5.** Photos showing tsunami damage on Sibigau Island, in the area of the profiles shown in Figure 4. (a) An aerial view, and (b) a ground-based view from the forest trimline at transect A of Figure 4, with the photo taken toward the northwest. The yellow marker on Figure 5a indicates the approximate field of view of Figure 5b.

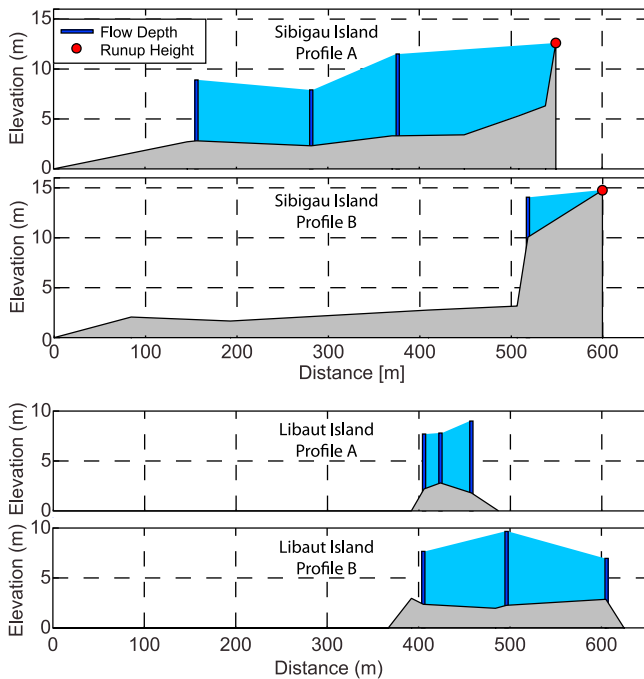


**Figure 6.** Characteristic tsunami survey transects: (top) Sibigau Island survey profiles from shoreline to runup heights, with locations shown in Figure 3; (bottom) South Libaut Island transects highlighting complete overwash by the tsunami.

[12] The first wave crashed over the boat and pushed it toward the back of the bay, causing his vessel to crash into the stern of another boat anchored in the bay that night. The two boats were pushed on to shore by that surge. A second surge re-floated the boats and allowed him to restart the

engines and orient the vessel seaward. The second boat had caught fire and was abandoned. While motoring toward the entrance of the bay, they were struck by a third wave that crashed over the bow of their boat.

### 3. GPS Data and Processing

[13] We processed the same SuGAR data twice, estimating both daily (averaged over 24-hr) solutions and instantaneous, high-rate (1-sec sampling) site positions, to best determine surface displacements due to the event. In the space-geodesy literature, the data processing methods involved in producing these two types of solutions are often referred to as static and kinematic, respectively. Under the assumption of no site motion, the daily solutions have the benefit of higher precision than the high-rate, which is largely achieved through data averaging. However, the 1-sec solutions have the advantage that they reveal the true coseismic signal, uncontaminated by postseismic deformation, and record both static displacements and seismic waveforms.

[14] To generate daily (static) solutions (Figure 7), we used the GAMIT/GLOBK software package [Herring *et al.*, 2005; King and Bock, 2005]. We used 15-sec data from the SuGAR as well as data products from the surrounding International GNSS Service (IGS) network to obtain daily solutions for station coordinates and other parameters, in a self-consistent local reference frame. Local solutions were combined with global IGS solutions, and around 150 core IGS stations were used to define the International Terrestrial Reference Frame (ITRF) 2005 reference frame [Altamimi *et al.*, 2007].

[15] To generate high-rate (kinematic) GPS solutions (Figure 8) we used the GIPSY-OASIS II v6.0 software package in Precise Point Positioning (PPP) mode [Zumberge *et al.*, 1997]. The kinematic processing scheme included estimation of time-varying station positions and tropospheric

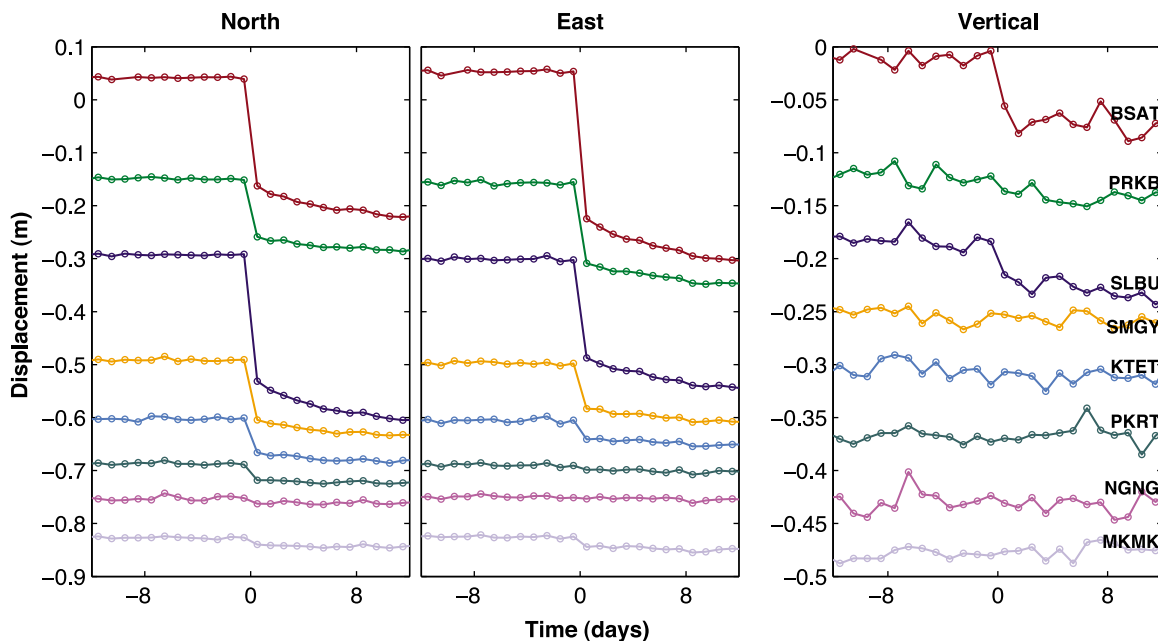


**Figure 7.** Three-dimensional GPS time series obtained from daily solutions, for a selection of near-field stations. Time at zero days is 25 October 2010. Note that the vertical time series have a different scale on the y-axis. Time series have been offset along the y-axis by an arbitrary amount, for clarity of illustration.

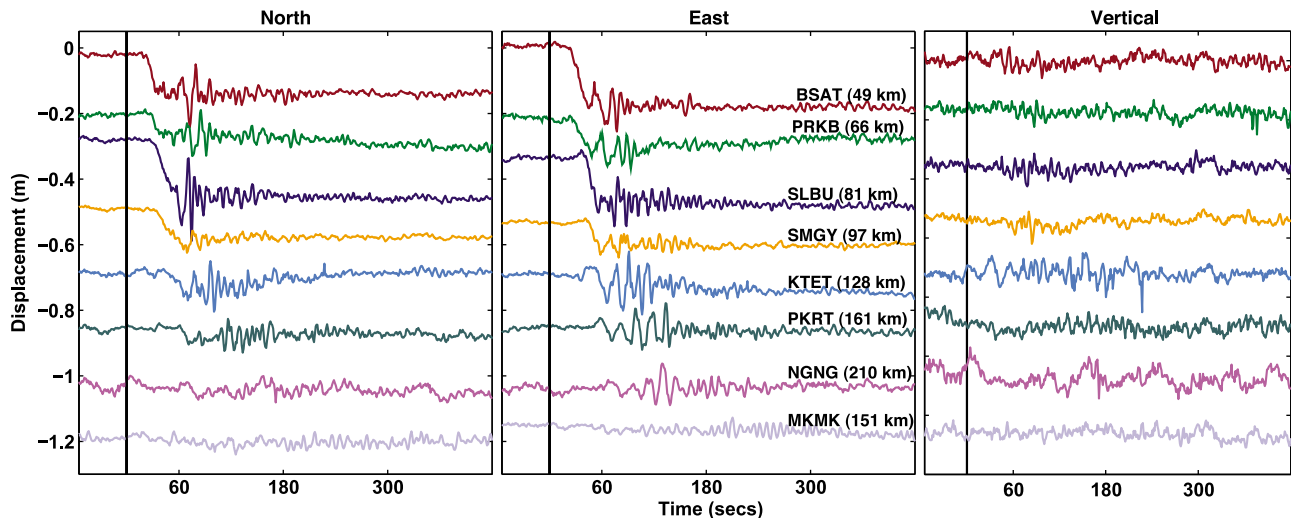


**Figure 8.** Three-dimensional GPS time series obtained from kinematic (1-sec) solutions. Sites and color code are consistent with those for Figure 7. The vertical black line indicates the time of the earthquake as estimated by USGS (with this being time 0 secs in the figure). The stations are ordered approximately south to north. Parenthesized distances are between the epicenter and the station. Time series have been shifted along the y-axis for clarity of illustration.

delays as stochastic random-walk processes, as well as resolution of carrier-phase ambiguities [Blewitt, 1989; Bertiger *et al.*, 2010]. We tested a range of values for the random-walk variance to ensure that site-position estimates were not biased by neither too-loose nor too-tight constraints [Elosegui *et al.*, 1996]. For the PPP approach, the satellite orbits and clocks were held fixed to precise values (we used the orbit and high-rate clock products from the Jet Propulsion Laboratory), so the station positions could be estimated independently in the ITRF2005 reference frame and are therefore not subject to errors inflicted by other stations in the network. The solutions were post-processed using a sidereal filter technique to reduce the effects of repeating, low-frequency, systematic errors such as multipath [Choi *et al.*, 2004]. Data for station KTET was, unfortunately, lost for the days preceding the earthquake due to a technical problem, so a sidereal filter was not applied for this station, resulting in higher levels of lower-frequency noise (and thus larger uncertainties in the offset estimate) for the 1-sec results for this site.

[16] Offsets for the static solutions (Table S1 in Text S1 of the auxiliary material) were estimated using 8 days of data before and after the main shock, using a simple least squares solution that includes both a Heaviside step function and a linear rate to account for any postseismic displacement in the days following the main shock. Quoted uncertainties (Table S1 in Text S1 of the auxiliary material) are GAMIT/GLOBK formal errors propagated through the least squares estimation. These are on the same order or slightly larger than the RMS of residuals about the least squares fit to the time series (the mean formal errors are 0.4, 0.3, and 1.0 cm for the East, North, and Up components, respectively, while the mean RMS residuals are 0.2, 0.2, and 0.6 cm).

[17] Offsets for the kinematic solutions (Table S1 in Text S1 of the auxiliary material) were estimated using 90 s of data either side of the earthquake, with the 2 min following onset of the earthquake removed to avoid the gradual

displacement of the stations (Figure 8). To better understand the uncertainty, we tested offset estimation using a variety of different lengths of time series between 1 and 5 min before and after the displacement. The maximum standard deviations in estimated offsets for each station was 0.5 cm in the horizontal and 1.0 cm in the vertical (at KTET), with mean values of 0.2 and 0.8 cm, respectively.

[18] For the kinematic solutions, we found that rather than estimating offsets individually at each site using the simple least squares procedure described above, a more spatially coherent solution could be obtained by first filtering the position time series using Principal Components Analysis (PCA) (for simple least squares estimation, coseismic displacement vectors for the noisier stations point in seemingly arbitrary directions, while this technique results in a spatially coherent and similar, but smaller, solution than that obtained from the static estimates). To implement this, we first ran a low-pass filter to remove the highest-frequency signals (this primarily affects the estimated uncertainties rather than the offsets), and then decomposed the filtered time series using PCA. Some examples of this are shown in Figure S1 in Text S1 of the auxiliary material. We next estimated the offsets using the time series based on only the first principal component of the filtered time series, which explains 99.9% of the variation present in the horizontal time series, and 88.0% of the variation in the vertical time series. To estimate uncertainties for the offset estimates, we calculated the weighted standard deviation of the low-pass filtered time series about the model.

[19] Comparison of the solutions reveals that horizontal coseismic displacements for the 1-sec solutions are considerably smaller than those for the 24-hr solutions. We calculated a scaling factor for the offset estimates of the static solutions, based on the horizontal kinematic solutions for stations BSAT, PRKB, SLBU, SMGY, and KTET, which are located in the near-field of the earthquake. A comparison of the scaled 24-hr solution with the 1-sec results is given in

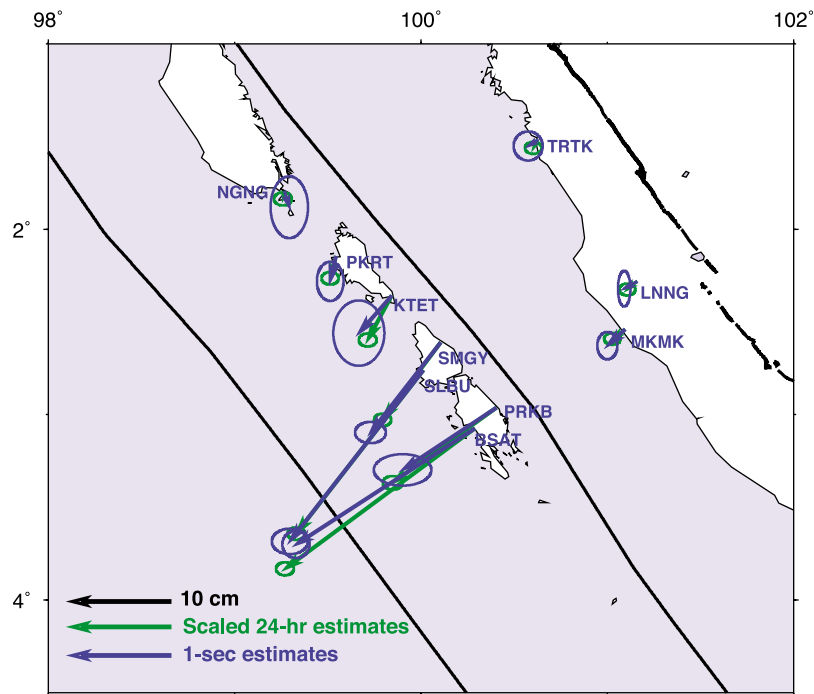


**Figure 9.** Comparison of static and kinematic coseismic horizontal offset estimates after scaling the former by 0.68.

Figure 9. The mean estimated scaling factor is 0.68, indicating that  $\sim 30\%$  of the displacement measured in the 24-hr solutions is likely to be from afterslip. Very rapid afterslip continued in the days and weeks after the earthquake, steadily diminishing through the time of this writing.

[20] The maximum horizontal displacement estimate (from the kinematic solutions) is  $22 \pm 0.5$  cm, at site BSAT,  $\sim 50$  km northeast of the epicenter. The kinematic solutions demonstrate that the rupture propagated from southeast to northwest (Figure 10, and Movie S1 of the auxiliary material), in good agreement with seismological results [Lay *et al.*, 2011]. The kinematic time series are dominated by surface waves, and suggest that the earthquake was quite deficient in high-frequency energy. This is in agreement with the seismological studies, which suggest that the soft sediments in this shallow environment inefficiently generate high-frequency energy, due to their low rupture velocity.

[21] One reason to estimate both static and kinematic solutions is that the kinematic results are noisy in the vertical component (Figure 8), and thus have large uncertainties in the vertical offset estimates. We calculated the scaling factor (described above) for the 24-hr solutions using only the horizontal results, but apply this to the vertical 24-hr solutions as well. A comparison of the scaled 24-hr results with the 1-sec estimates, for the vertical component, is given in Figure S2 in Text S1 of the auxiliary material. We see significant differences between the scaled 24-hr and 1-sec vertical offset estimates, e.g., a difference of 4.1 cm at station BSAT (Table S1 in Text S1 of the auxiliary material).

[22] Based on the scaled 24-hr results, the largest vertical displacement was  $-4 \pm 1$  cm, at station BSAT. The 24-hr solutions consistently indicate subsidence at all nearby sites. We note, however, that there are additional uncertainties in the scaled 24-hr solutions due to our assumption that the

ratio of horizontal to vertical postseismic deformation will be the same (this may not be the case if the afterslip is in a different location to coseismic slip). Based on this uncertainty, and the large error bars on the kinematic solutions, we cannot rule out zero vertical displacement at the nearby sites. It seems unlikely, however, that the vertical coseismic displacement was in an upwards direction.

[23] Both the horizontal and vertical values are considerably smaller than one might expect to be associated with a source that produced such a large tsunami. They are also far smaller than predicted in previous studies that inverted only seismological data to get the measured tsunami parameters. Newman *et al.* [2011], for example, calculated a finite-fault solution from teleseismic data and scaled the source upward by an average of 5.6 times to get seafloor displacements great enough to reproduce the observed tsunami effects. They justified the scaling by assuming the rocks of the shallow megathrust have a low rigidity, thus requiring greater slip to produce the measured  $M_w$ . However, their source model produces unrealistic static geodetic displacements (subsidence for parts of the Mentawai coast of  $>0.5$  m, and horizontal displacements of  $>1$  m), far greater than we observed.

#### 4. Tsunami Modeling

[24] We used the Cornell Multigrid Coupled Tsunami Model (COMCOT) software package [Liu *et al.*, 1994] to model tsunami generation, propagation, and inundation. COMCOT simulates the tsunami propagation and inundation by solving nonlinear shallow water equations using an explicit leapfrog finite difference method on nested grids. Up to 12 levels of nested grids can be used to obtain detailed information in specific regions of interests. We used 8 nested grids (Figure S3 and Table S2 in Text S1 of the auxiliary

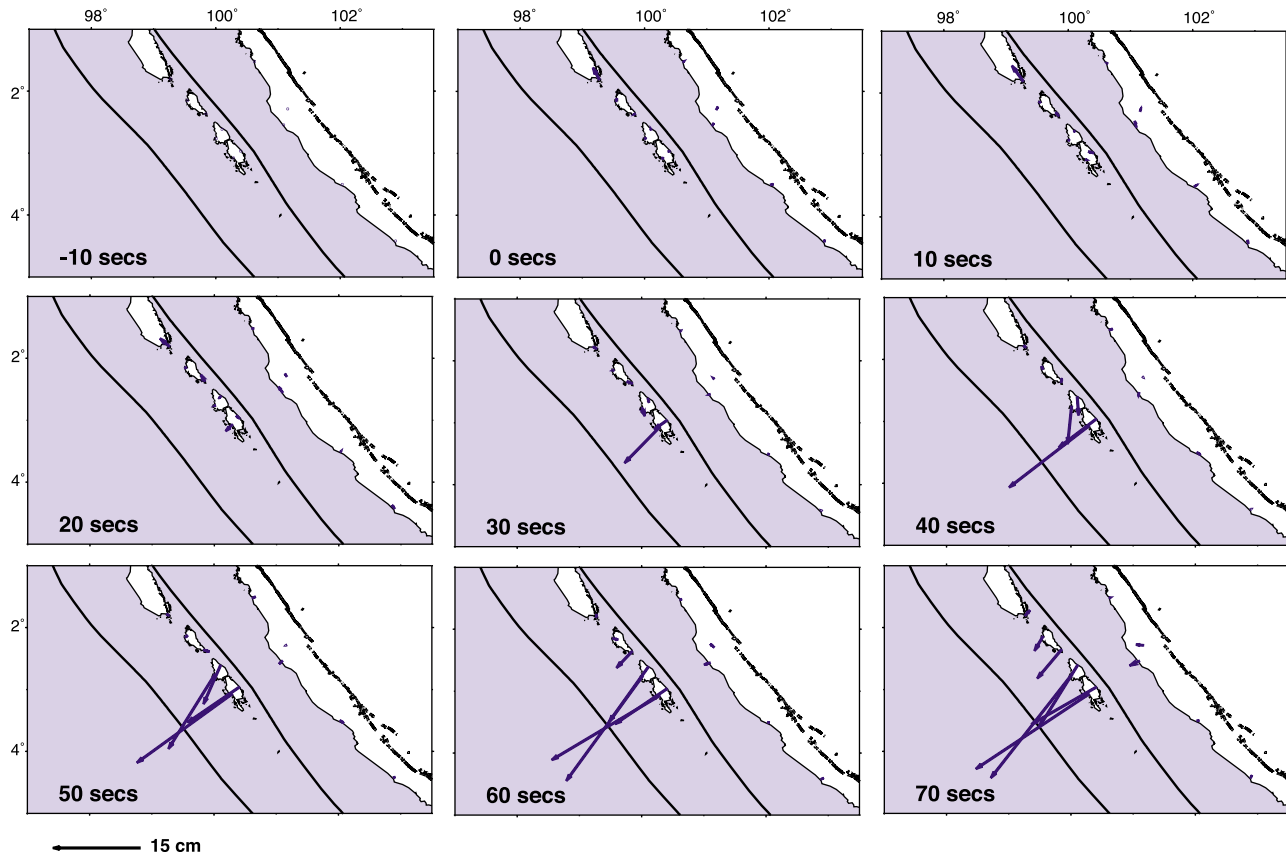


**Figure 10.** GPS horizontal displacements at 10-second intervals, indicating southeast to northwest propagation of the rupture. The displacements are cumulative, relative to a time 10 s before the USGS-estimated time of the earthquake. High-frequency signals, including the seismic waveforms, were first removed from the time series using a low-pass filter.

material), to obtain higher resolution in shallow water regions.

[25] Since the propagation of tsunamis is strongly affected by bathymetry and topography, we combined the most accurate bathymetric and topographic information available, as described below (and made available in the auxiliary material). Inaccuracies in these data sets remain, however, one of the primary sources of uncertainty in our modeling.

[26] For the deep-water bathymetry, we used the 30 arc-second ( $\sim 925$  m) gridded bathymetric data from the General Bathymetric Chart of the Oceans (GEBCO) [<http://www.gebco.net>]. The GEBCO data were generated using a combination of quality-controlled ship depth soundings and satellite gravity data.

[27] Topographic data were taken from the NASA Shuttle Radar Topographic Mission (SRTM) [<http://www2.jpl.nasa.gov/srtm>] with 3-arcsecond resolution ( $\sim 90$  m). The vertical accuracy in the SRTM data is stated as  $\pm 16$  m at the 90% confidence level [Hayakawa *et al.*, 2008; Smith and Sandwell, 2003]. Large errors in the ground elevation from SRTM may exist in the regions where terrain is covered by dense vegetation [Van Niel *et al.*, 2008]. The vertical accuracy is also terrain-class dependent, with steeply sloping regions having greater mean error than flatter surfaces. In areas of interest for detailed hydrodynamic modeling, we corrected the SRTM data using topographic information collected during the field survey. Such corrections were

made for Sibigau, Libaut, Tumalei and Sabeugukung. Some corrections were on the order of  $\sim 10$  m, and reflect the fact that the SRTM data sometimes correspond to the top of the palm trees, rather than to the ground. The corrections were done by manually manipulating the topography data to reflect the shape of the cross-shore profiles we measured in the field.

[28] Since there is an overall lack of bathymetric data in shallow water, data gaps between the bathymetry and topography were interpolated and filled using digitized nautical charts, for water depths up to 200 m. Digitized charts were reprojected from UTM Batavia/Bessel 1841 to WGS84 prior to use.

[29] A practical issue in combining these three data sets is the determination of the shorelines. In this study, the shorelines specified by the SRTM Water Body data set [<http://www2.jpl.nasa.gov/srtm>] were used to distinguish the land-mass and the water body when combining GEBCO and SRTM data. The SRTM Water Body data were created by the U.S. National Geospatial-Intelligence Agency through identification and delineation of ocean, lake, and river shorelines in the SRTM data, which were then set to constant values to create the final SRTM Digital Elevation Terrain data. We also adjusted our digitized shorelines from the nautical charts using these SRTM Water Body data.

[30] Finally, we interpolated the bathymetric and topographic data to a spatial resolution of 41.1 m for input to the

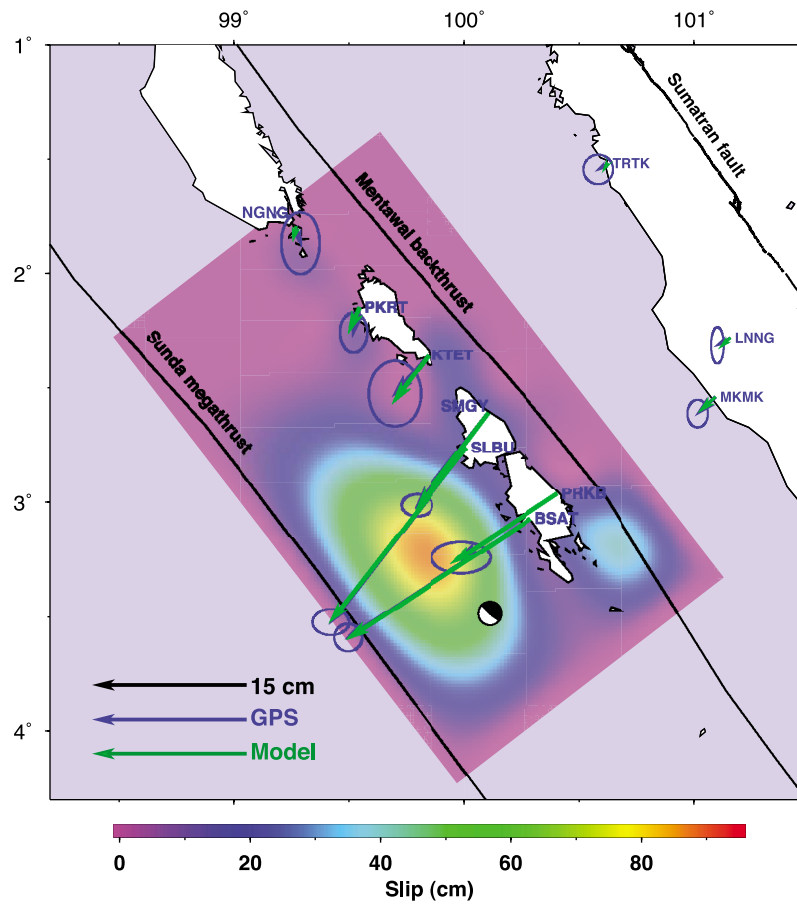


**Figure 11.** Slip distribution from an inversion of the GPS displacements that did not contain prior slip constraints, giving an indication of the maximum slip possible if the rupture patch is closer to the islands. This slip distribution is unable to produce the measured tsunami, and ignores model resolution problems.

tsunami modeling calculations. This is approximately half the resolution of SRTM.

[31] The tsunami models were initiated using vertical coseismic displacements of the seafloor on a high-resolution grid. These were calculated using a forward model with Green's functions for a layered elastic crust [Wang *et al.*, 2003] and the slip distribution obtained as described in section 5. Although we initially calculated uplift values on a  $0.01^\circ$  grid, they were further interpolated and smoothed to the very dense coordinates of the high-resolution tsunami grid.

## 5. Modeling of Coseismic Slip Distribution

[32] To invert the GPS estimates of surface deformation for coseismic slip distribution, we employed standard linear inversion techniques for an assumed, planar, fault geometry [Harris and Segall, 1987; Du *et al.*, 1992]. Our model fault has a strike of  $322^\circ$ . We fixed the dip to a constant value of  $7^\circ$  and the rake to  $98^\circ$ , as estimated in the Global Centroid Moment Tensor solution [http://www.globalcmt.org]. (In the light of limited resolution and relatively small rupture area, it does not seem sensible to double the number of unknown parameters by allowing the rake to vary.) The down-dip edge of our fault model has a depth of 20 km, although all slip appears to occur considerably shallower than this, with the majority at depths  $>6$  km.

[33] We based our inversions of GPS data for coseismic slip distribution on Green's functions calculated using the EDGRN/EDCMP code from Wang *et al.* [2003], using a horizontally layered crustal structure based on interpolated values for the CRUST 2.0 model [http://igppweb.ucsd.edu/~gabi/crust2.html] (Figure S4 in Text S1 of the auxiliary material). The CRUST 2.0 crustal model is quite coarse, but allows for more realistic gradients in the elastic structure than if we used a simple elastic half-space (i.e., single layer) model based on the Okada [1985] formulation. Many previous studies of tsunami earthquakes, and many tsunami-modeling studies, have used the Okada [1985] formulation to calculate seafloor displacements, but our tests show that for shallow tsunami earthquakes, where gradients in rigidity can be high, the use of a layered crustal structure is important.

[34] We used a finite difference Laplacian smoothing matrix to impose smoothness constraints on the model, to regularize the inversion. We also employed a non-negativity constraint [Lawson and Hanson, 1974], with the assumption that no backslip should be accommodated in the earthquake, and constrained the slip to zero along the sides and bottom of the fault patch.

[35] An inversion using only the GPS static displacements produces maximum coseismic slip of 86 cm, based on a fault with dip of  $7^\circ$  (Figure 11). For this inversion we estimated a

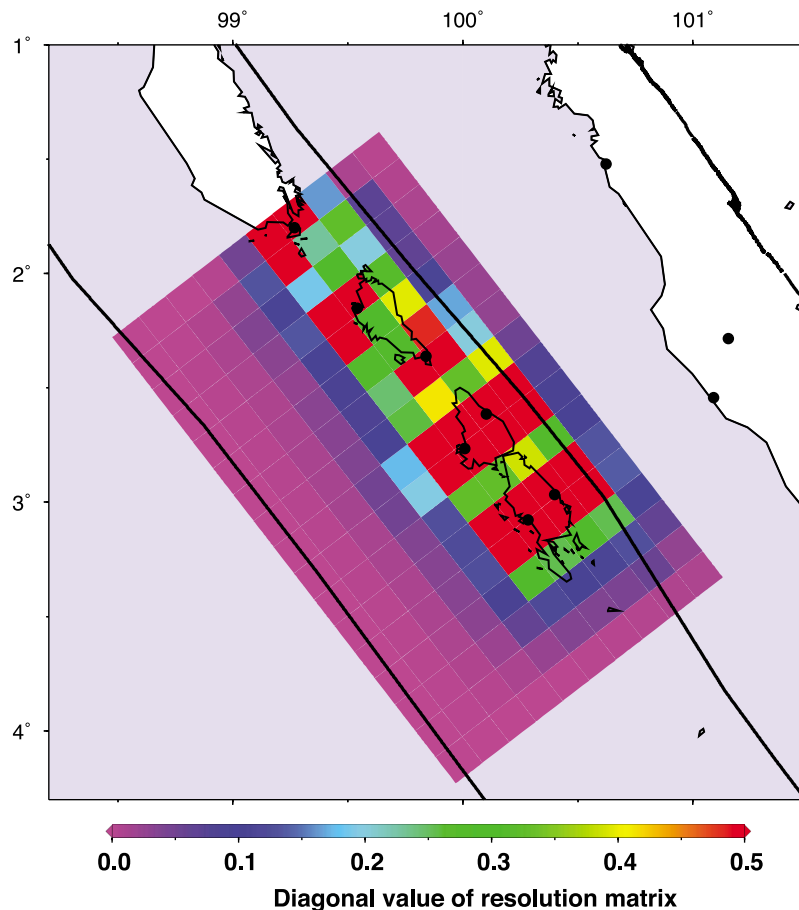


**Figure 12.** Color-coded values of the diagonal elements of the resolution matrix for each fault patch. The color bar saturates at 0.5, instead of 1, to highlight lower values. To calculate the resolution matrix we used the same smoothing weight as estimated for the unconstrained GPS inversion, which was chosen based on examination of a trade-off curve between residuals and model roughness. Black dots indicate GPS station locations.

weighting parameter for the Laplacian smoothing using a tradeoff curve between data misfit and model roughness. This results in maximum seafloor uplift of  $<15$  cm. Regardless of possible inaccuracies in the topography and bathymetry used for tsunami modeling, seafloor uplift of this magnitude is incapable of producing tsunami runup of  $>6$  m. This model also underestimates the earthquake's magnitude, at  $M_w \sim 7.5$ .

[36] Inversion of GPS displacements for coseismic slip distribution, however, is usually a highly ill-posed problem. To estimate variable slip across a fault, it is divided into a number of individual patches, or sub-faults, with many more estimated parameters than observations. Several recent studies have illustrated the importance of considering the model resolution matrix when deciding on an appropriate sub-fault size [Page *et al.*, 2009; Barnhart and Lohman, 2010]. The model resolution matrix characterizes whether slip on an independent sub-fault can be uniquely determined. In equation (1), if the resolution matrix ( $R$ ) is not an identity matrix (i.e., poor model resolution), then the estimates of the model parameters ( $m_{est}$ ) will be weighted averages of the true model parameters ( $m_{true}$ ) [Menke, 1989]. In the case of

inversion for a slip distribution, the true slip on a sub-fault will be averaged over many sub-faults:

$$m^{est} = Rm^{true} \quad (1)$$

Worryingly, if slip occurs in an area without good model resolution, it can introduce spurious features into the solution [Page *et al.*, 2009]. The slip for our study appears to have occurred at considerable distance from the stations, so this problem could be significant.

[37] An illustration of the diagonal elements of our resolution matrix is given in Figure 12. Ideally, these values should all be unity, so it is clear that we have limited resolution at very shallow depths. We also show, to further illustrate this point, inversions of synthetic slip models for deep and shallow slip on our fault patch (Figure 13). These tests indicate that we cannot 'see' more than  $\sim 20\%$ , at most, of slip for the shallowest part of the fault. The magnitude  $M_w$  for the synthetic slip distribution is 7.4, whereas the recovered  $M_w$  for the deep and shallow tests is 7.4 and 7.0, respectively (with rigidity set to a constant 30 GPa for

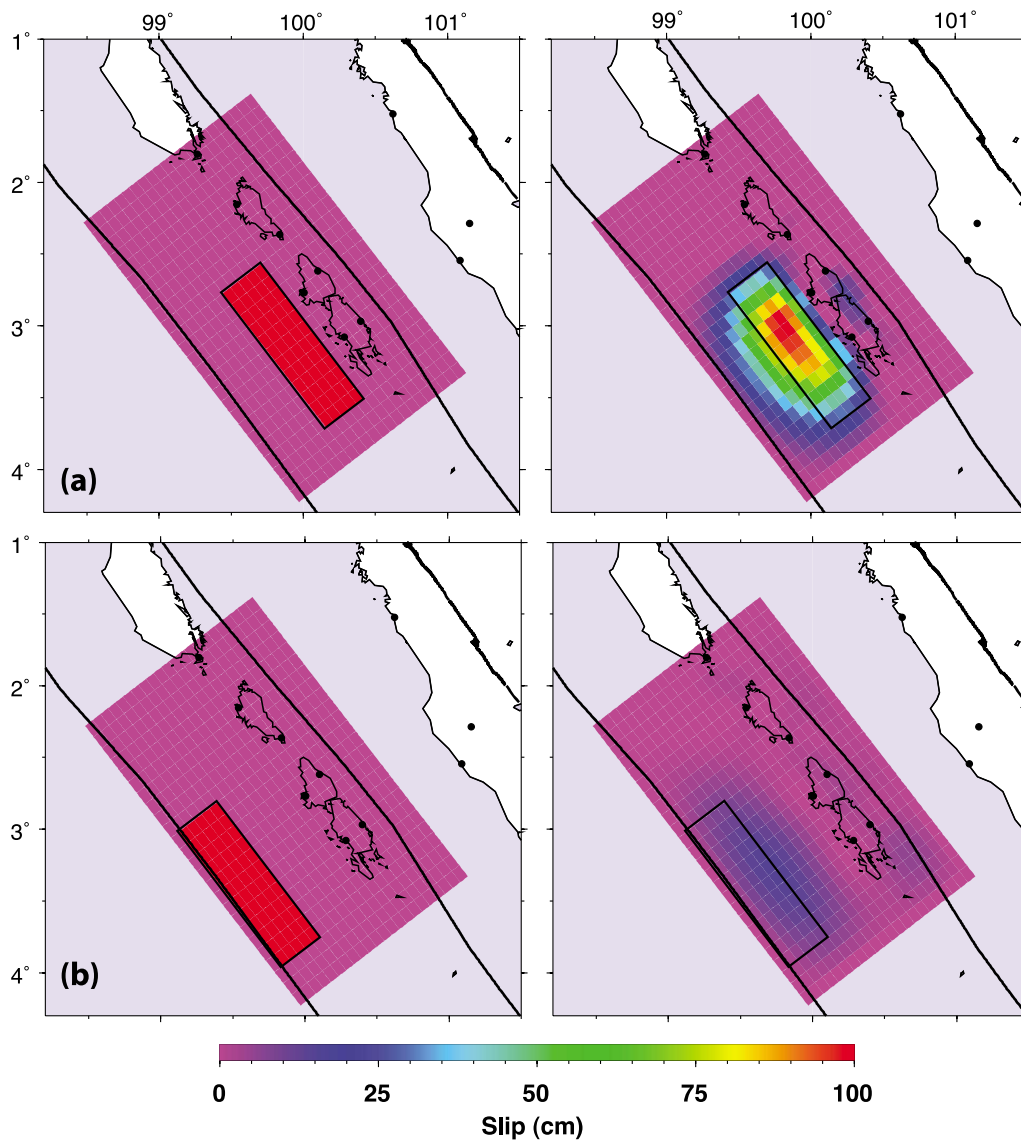


**Figure 13.** Checkerboard-type test for a synthetic fault rupture located (a) close to the Mentawai Islands (i.e., a deeper rupture) and (b) at shallow depth. The left-hand panel shows the input model, which has uniform slip of 100 cm, while the right-hand panel shows the results of inverting synthetic displacements from this model. Black dots indicate GPS station locations. The test indicates that the inversion can only resolve ~20%, at most, of slip in the area of the fault very close to the trench.

the  $M_w$  calculations for this test, for ease of comparison). Checkerboard-type studies made for previous studies in the area [Konca *et al.*, 2008; Chlieh *et al.*, 2008; Hsu *et al.*, 2006], have also illustrated the low resolution in this very shallow area. It is therefore possible that large amounts of slip can occur in the shallow area of the fault, in the area between the trench and the midpoint between trench and islands, that would not be fully detected by the GPS.

[38] The diagonal elements of the model resolution matrix could be made closer to unity by increasing the size of the sub-faults. However, larger sub-faults will smooth any highly concentrated slip occurring within the area of a sub-fault. Since the tsunami may have been caused by highly concentrated slip, this could give misleading results. We therefore use sub-faults that we know are smaller than our model

resolution will allow, but apply a priori slip constraints to the GPS inversion, based on the fault slip that is needed to produce a tsunami model that agrees with our tsunami data. This means that we use the inversion to estimate adjustments to an a priori slip model, resulting in a model with predicted GPS displacements that fit the observations, while also keeping the slip as close to the a priori distribution as possible. The level of adjustment allowed in the inversion is constrained by the uncertainties placed on the a priori slip distribution. Initial tsunami-modeling tests, using simple source models, suggested that at least 2 m of vertical seafloor deformation, extending along strike for ~100 km between North and South Pagai, is necessary for the hydrodynamic model results to approach the observed tsunami effects.

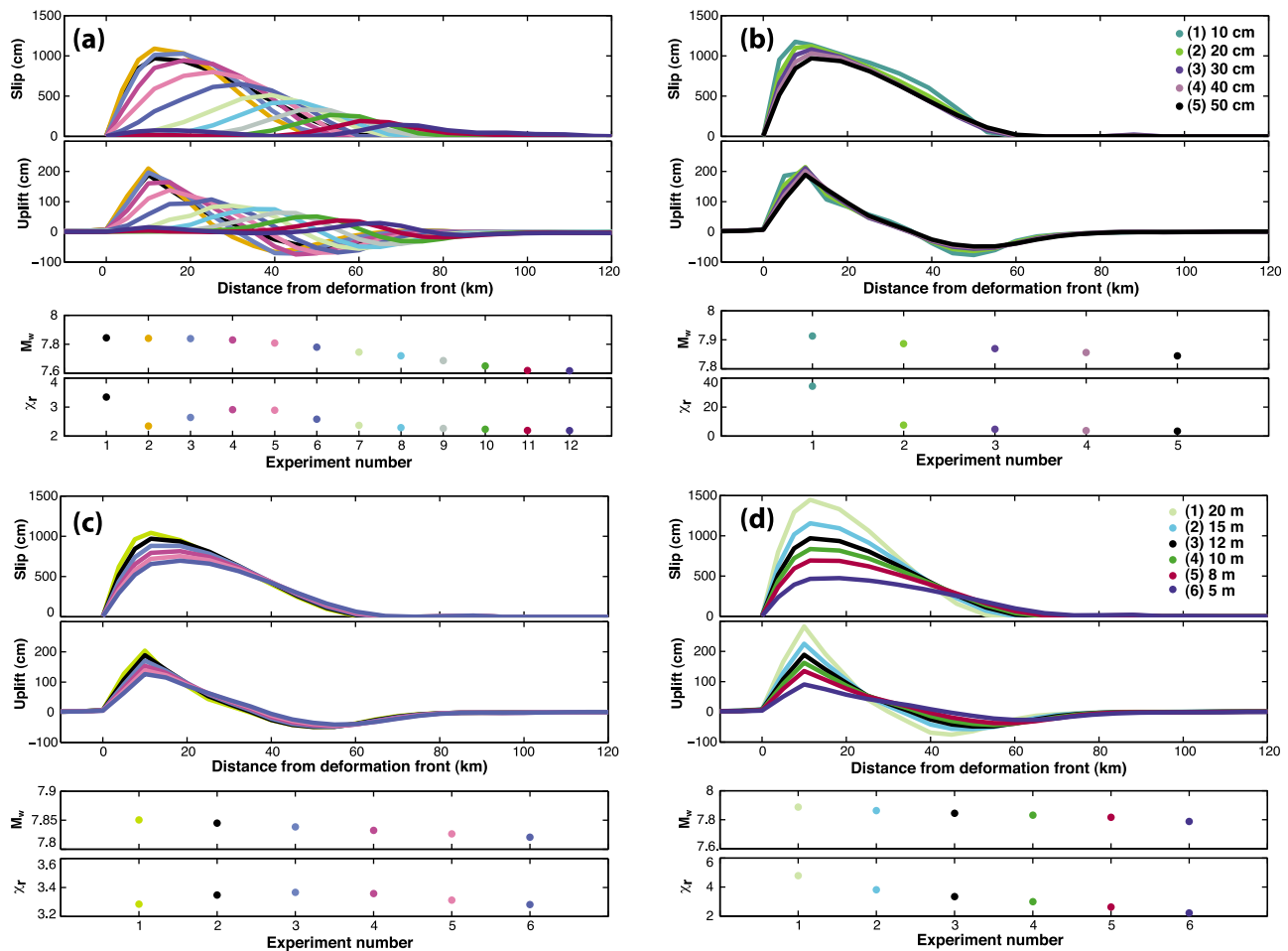


**Figure 14.** Examples of slip and surface uplift profiles, plotted along a SW-to-NE profile perpendicular to the trench, resulting from variations in the model constraints. Also given are estimates of moment magnitude,  $M_w$ , and the weighted mean of the sum of squares residuals,  $\chi_r$  (see explanation in section 5). Note that all profiles are plotted through the area of highest slip, and that rupture patches close to the trench become very small in area (e.g., see  $M_w$  estimates for Figure 14a). All models result in a similar fit to the GPS data. Our preferred model is shown in black, for all panels. For all tests, all parameters were set to those for our preferred model, except for the parameter that is indicated, as follows: (a) Experiment 1 refers to the preferred model. The rest of the tests are for an a priori slip patch with fixed width, with each test moving the patch further downdip. (b) Variations in the standard deviation of a priori slip, as given in legend. (c) Variations in the degree of smoothing (from less to more smoothing with increasing experiment number). (d) Variations in the amplitude of a priori slip (applied for a width of fault between the trench and islands), as given in legend.

[39] When applying a priori slip constraints, we also used smoothing constraints to ensure that the slip tapers from its maximum value to zero slip in a physically reasonable way. The a priori slip distribution consists of constant slip over a rectangular area, with zero slip around the edges of the rectangular patch, but we do not want the resulting distribution to have such sharp gradients. Examination of a wide variety of published slip distributions indicates that slip ( $s$ ) usually decays over a distance ( $d$ ) following equation (2), with, approximately, average values of  $x$  around 3.7 and a range of  $\sim 3.0$  to 4.2. We therefore used our smoothing constraints to ensure values of  $x$  close to this. We also allowed asymmetric smoothing, through modification of the distance weighting, allowing smaller values of  $x$  on the updip side (as the rupture approaches the sedimentary wedge). Values of  $x$  for our

preferred model are 3.1 on the updip side, and 3.8 on the downdip side:

$$d = 10^x s \leftrightarrow x = \log_{10} \left( \frac{d}{s} \right) \quad (2)$$

[40] The use of a priori constraints is, of course, somewhat ad hoc, and depends heavily on the uncertainties placed on both model and data. We therefore conducted many tests to investigate the effects of these constraints. Figure 14 shows slip and uplift profiles obtained as a result of varying the prior constraints in four different ways (area of slip involved, a priori slip uncertainties, smoothing, and a priori slip amplitude), as well as estimates of  $M_w$  and the weighted mean of

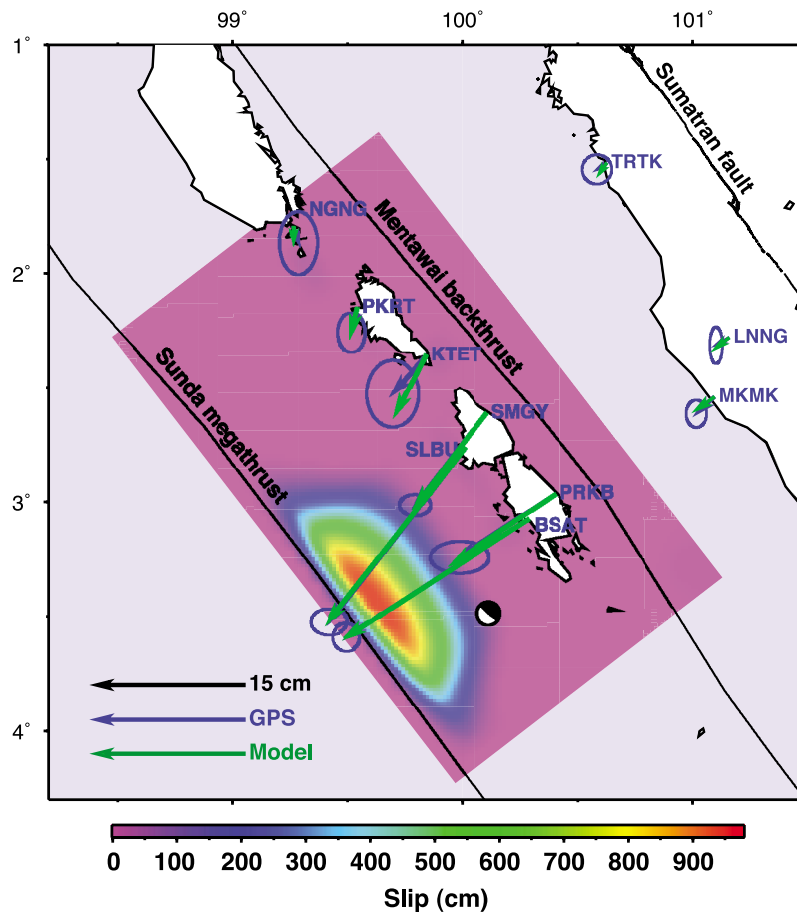


**Figure 15.** Horizontal coseismic offsets from GPS (vectors) and surface projection of preferred slip distribution model. Error ellipses are 99% confidence. Vertical displacements are given in Figure S7 in Text S1 of the auxiliary material. The megathrust trace is from *Bird* [2003], which approximately coincides with the deformation front (above the end of the blind megathrust at 1.5 km depth) of *Singh et al.* [2011]. In our modeling, the fault between 0 and 1.5 km depth is constrained not to slip.

the sum of the squares of the residuals. This latter value is similar to a reduced chi-square value, except that it involves the number of observations instead of the number of degrees of freedom. (It is not possible to use the reduced chi-square itself, in part because we cannot reliably estimate the number of degrees of freedom in the presence of constraints. However, since the number of observations and solved-for parameters remains the same in all experiments, it is indicative of goodness-of-fit.) Our goal was to find a model that provided highest levels of seafloor uplift, while maximizing the fit to the GPS data and producing  $M_w \sim 7.8$ . We also paid attention to producing a physically reasonable level of slip tapering, as discussed above, and required subsidence or zero vertical displacements for the local stations. To ensure that the model would still result in a good fit to the GPS displacements, rather than being dominated by the a priori slip constraints, we scaled the GPS uncertainties by 0.4, although larger uncertainties do not significantly change the results (Figure 14c). Of all the constraints, changes in the location of the a priori slip patch results in the greatest changes to the resulting model (Figure 14a).

[41] Our layered elastic model will allow higher levels of slip in the shallow area of the fault, while still fitting the GPS data, compared to those from a half-space model (Figure S5

in Text S1 of the auxiliary material). The layered model also allows for a broader slip and uplift patch. Additional slip and seafloor uplift could be possible with sharper gradients in local rigidity than the CRUST2.0 model gives, but we do not test this, given our limited resolution.

[42] For our preferred model (Figure 15) we use an a priori slip distribution of  $12.0 \pm 0.5$  m on an area with length 120 km and width extending from the trench to the islands. The inversion adjusts slip in the area that the GPS can “see” back down to much lower values than the prior ones.

## 6. Fault Geometry and Inelastic Sediment Uplift

[43] We use megathrust geometries that are consistent with those seen in recent seismic reflection profiles nearby [*Singh et al.*, 2011]. These show conclusively that the megathrust does not break through the seafloor. Rather, it is a shallow-dipping blind thrust fault that has propagated along the base of the sedimentary prism to a position about 1.5 km below the trench axis.

[44] With their steeper dip, splay faults are more effective at producing high values of seafloor uplift, and have therefore been proposed as a possible mechanism for several past tsunami earthquakes [*Cummins and Kaneda*, 2000; *Moore*

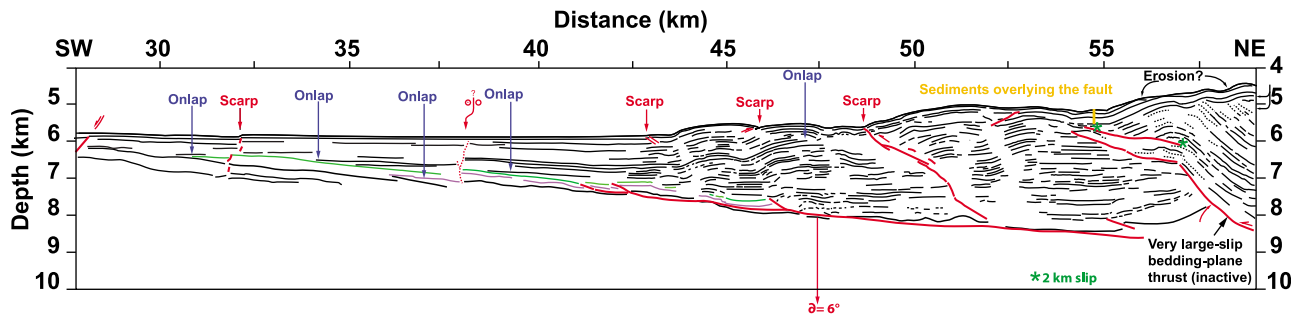


**Figure 16.** Our interpretation of the seismic reflection profile of *Singh et al.* [2011] shows that the sediments above the Sunda megathrust in the vicinity of the October 2010 rupture are only mildly deformed in the 12 km nearest the trench. This means that slip on faults breaking the sedimentary wedge is minor, compared to slip on the megathrust itself. Faults appear in red; sedimentary reflectors appear in black. Onlaps of trench sediment show the most recent history of filling of the trench. Steep dips on two faults southwest of the trench axis (42.5 km) suggest that their sense of slip is strike-slip. The fault near the surface at km 55 has been inactive for a long time, as evidenced by the fact that its trace is buried by about 400 m of sediment. In the text we calculate that slip on the megathrust at km 47.5 is only about 700 m, which may have accrued in just the past 16,000 years. Slip on the fault at km 55 is about 2.2 km, which may have accrued in the past 49,000 years. The slip patch for our preferred model falls over the area between approximately km 43 to 55.

*et al.*, 2007; *Wendt et al.*, 2009]. We cannot rule out the action of a splay fault from the GPS results. However, reexamination of the seismic profiles published by *Singh et al.* [2011] indicates to us that shallow splay faults in this area are not presently active. Rather, the seismic profile shows that slip on the megathrust has resulted in folding and uplift of the trench sediments within 12 km of the deformation front. A figure showing the original seismic profile is given in *Singh et al.* [2011, Figure 2]. Our interpretation is given in Figure 16.

[45] Mild folding of sediments within 12 km of the deformation front (km 43 to 55 in Figure 2 of *Singh et al.* [2011]) implies that the megathrust lies at the base of the folds, atop the oceanic basement, and has experienced little total slip. Our preferred coseismic slip model occurs over this same area. The greatest deformation of the accreting sediments occurs between km 55 and 58, where sediments have run up and over a fault ramp about 2.5 km. This fault within the accretionary wedge appears, however, to be inactive, because it does not cut the youngest 400 m of sediment.

[46] Slip on the megathrust trenchward of the inactive fault has resulted in folding of trench sediments, dominated by three anticlines ranging in width from about 2 to 6 km and accompanied by minor faulting. A mass balance calculation implies that total slip on the megathrust at km 55 has been about 2.2 km. We calculate this value by determining that the sediment that lies above a line extrapolated northeastward from the top of the undeformed sediment has a cross-sectional area of about 5.6 km<sup>2</sup> (an annotated diagram is available in Figure S6 in Text S1 of the auxiliary material). This sediment should roughly equal the pre-deformation thickness of the wedge at km 55 (2.6 km) times slip on the megathrust. Thus, one derives about 2.2 km of shortening over the life-span of this youngest 12-km section of the megathrust. A similar calculation for total slip on the megathrust at km 47 yields just 700 m of total slip. At a rate of convergence of 4.5 cm/yr, the megathrust would have begun to propagate southwestward past km 55 about 49,000 years ago and past

the km 47 mark about 16,000 years ago. Thus, the age of the section of the megathrust that caused the earthquake and tsunami is very young.

[47] Compared to the amounts of slip on the megathrust, slip imaged on the minor fault at the deformation front is miniscule, only a few tens of meters. Thus, it is reasonable to conclude that this minor fault that forms a 40-m scarp on the seafloor is a minor feature and not the primary source of the 2010 earthquake and tsunami, contrary to the interpretation of *Singh et al.* [2011]. Instead, the presence of seafloor anticlines in the profiles suggests that, in addition to blind, elastic rupture of the megathrust, there was concomitant inelastic, permanent bulging of the overlying seafloor. This has been proposed in the past as a possible mechanism for tsunami earthquakes, through a process that can be thought of as similar to that of a bulldozer pushing up a pile of sand [*Seno*, 2000; *Tanioka and Seno*, 2001].

## 7. Modeling Results

[48] Our preferred coseismic slip model (Figure 15) is the result of placing prior slip constraints of  $12.0 \pm 0.5$  m on a large patch of the megathrust between the trench and the islands. In the area close to the islands the model iteratively adjusts to accommodate the small displacements observed by the GPS. That is to say, any large patch of slip >4 m must be accommodated in a very shallow and narrow strip of the megathrust, at depths <6 km and no further than ~50 km from the trench. Maximum slip for our preferred model is 9.7 m, and maximum seafloor uplift is 1.9 m, although many other models are of course possible. This model produces a magnitude of  $M_w \sim 7.8$ , based on rigidity values from the regional model for crustal structure.

[49] A comparison of modeled and measured tsunami runup resulting from our preferred model is shown in Figure 17. This model comes much closer to predicting the measured tsunami than the model produced using no prior slip constraints (Figure 11), although the majority of constrained

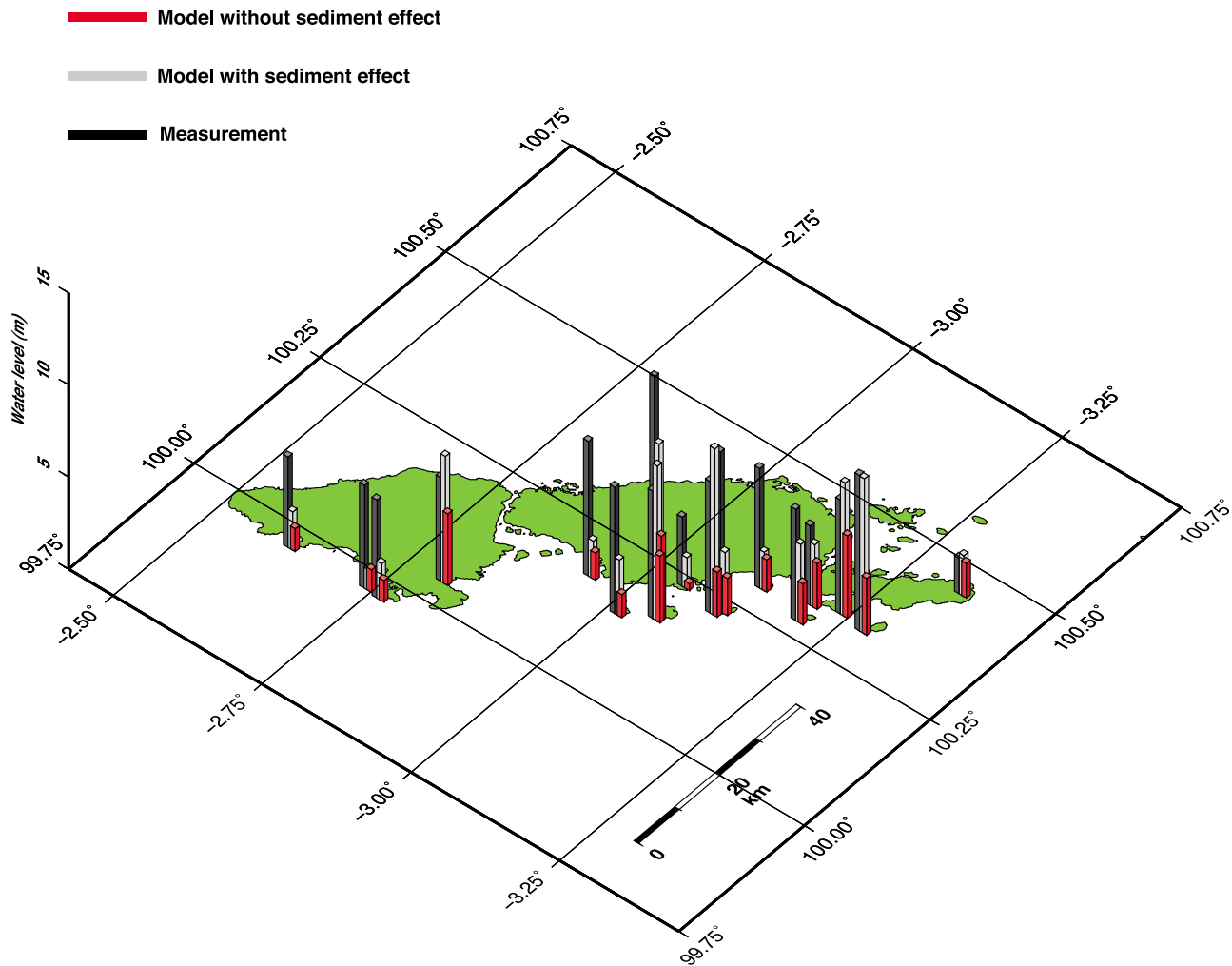


**Figure 17.** Spatial distribution of the water level measurements from the October 2010 Mentawai tsunami (black bars), and modeled runup heights based on our preferred slip distribution, with and without additional inelastic uplift included (gray and red bars, respectively). Not all measurements have been included in the figure, for clarity of illustration. Although the water-level scale saturates at 15 m, some measurements were higher than this.

models still underestimate runup in many places. It is likely that some of this misfit is due to errors in the bathymetry and topography used for tsunami modeling, complexities in the fault rupture that we are not able to resolve, and heterogeneities in the Earth structure that are not included in our model [Hsu *et al.*, 2011]. Indeed, underprediction of field measurements is to be expected. Depth-integrated hydrodynamics is known to underpredict field observed runup, particularly for large scale, chaotic and turbulent flows that cannot be modeled with grids larger than meter-scale; a prohibitive undertaking for field-scale simulations. Small-scale coastal features not represented in our models are known to affect runup heights, sometimes to first order [Kanoglu and Synolakis, 1998]. Notable underprediction of runup at Sigibau may be due to unmodeled complexities in the hydrodynamics from the steep topography (Figure 6). Resonant amplification, recently identified along a single 2-D bathymetric transect [Stefanakis *et al.*, 2011], could also contribute to enhanced runup for a particular amount of seafloor deformation, although our modeling includes the

entire waveform and should have captured such amplification, if still existent in three-dimensional propagation. Adding to these uncertainties, field measurements are often biased toward extreme values.

[50] This model also underpredicts recordings from the DART seafloor pressure sensor (station 56001) located  $\sim 1600$  km to the SE of the rupture (Figure 18). Figure 18 also illustrates the importance of using a layered elastic model for the deformation calculations (section 5), as the half-space model results in significant underprediction of the DART record due to its narrower uplift patch (Figure S5 in Text S1 of the auxiliary material).

[51] To correctly include an additional inelastic sediment effect (section 6), we would require additional modeling, with incorporation of an elastoplastic response of the shallow material to rupture. For a rough, and ad-hoc, first estimate, however, we tested the effects of placing an additional 2.5 m of uplift over the width of the imaged anticlines. Our simple model consists of adding the extra uplift to a rectangular patch of width 11 km and length 43-km, above the area

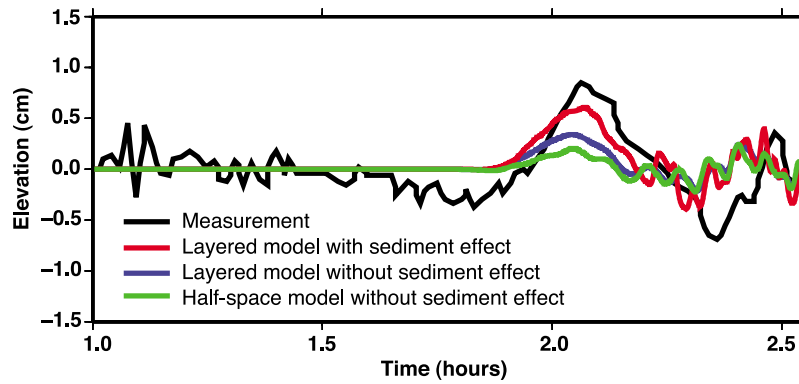


**Figure 18.** Comparison of modeled tsunami wave with the DART ocean-pressure sensor record (station 56001), based on our preferred models, with and without additional inelastic sediment uplift included. Models indicated as “layered” are based on our preferred source model. The half-space model was based on a source model that uses Green’s functions from the Okada formulation (also chosen to give the highest uplift and  $M_w$  7.8, while still fitting the GPS).

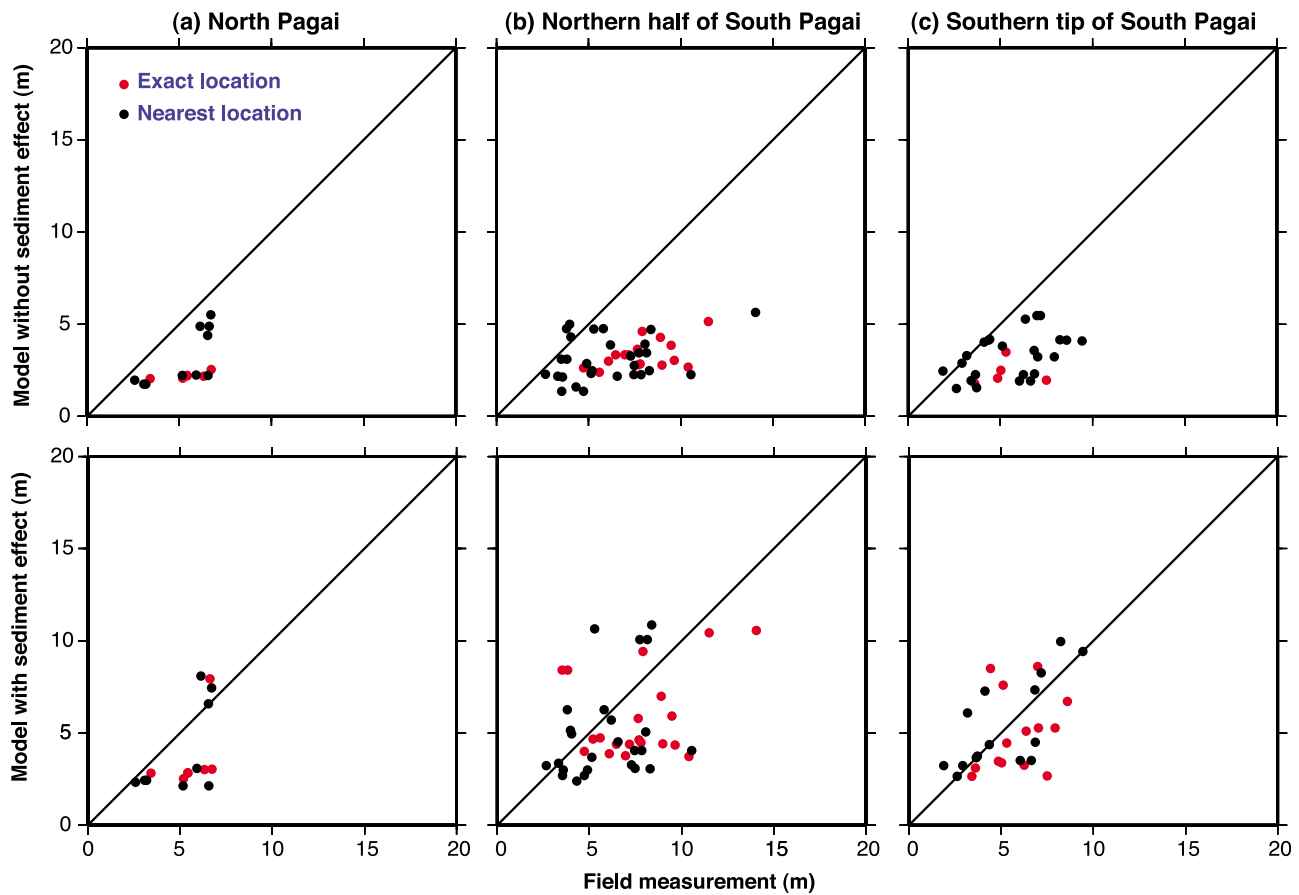


**Figure 19.** Comparison of tsunami survey data and model runup heights. The diagonal lines indicate where the points would lie if there was perfect agreement between model and data. The tsunami model was initiated with the source model shown in Figure 15, with (bottom) and without (top) the model for inelastic sediment uplift included. Red dots indicate locations where a tsunami model point was available at the same location as the field measurement, while black dots indicate locations where the nearest model grid point to the field location was used. The three columns are for locations (Figure 3) from (a) Tumalei to Sabeugukung (Grids 2c, 2d, 2e in Figure S3 in Text S1 of the auxiliary material), (b) Siopasabeu to Siumang (Grids 2b, 2f, 2g) and (c) Limoksua to Lighthouse (Grid 2a).

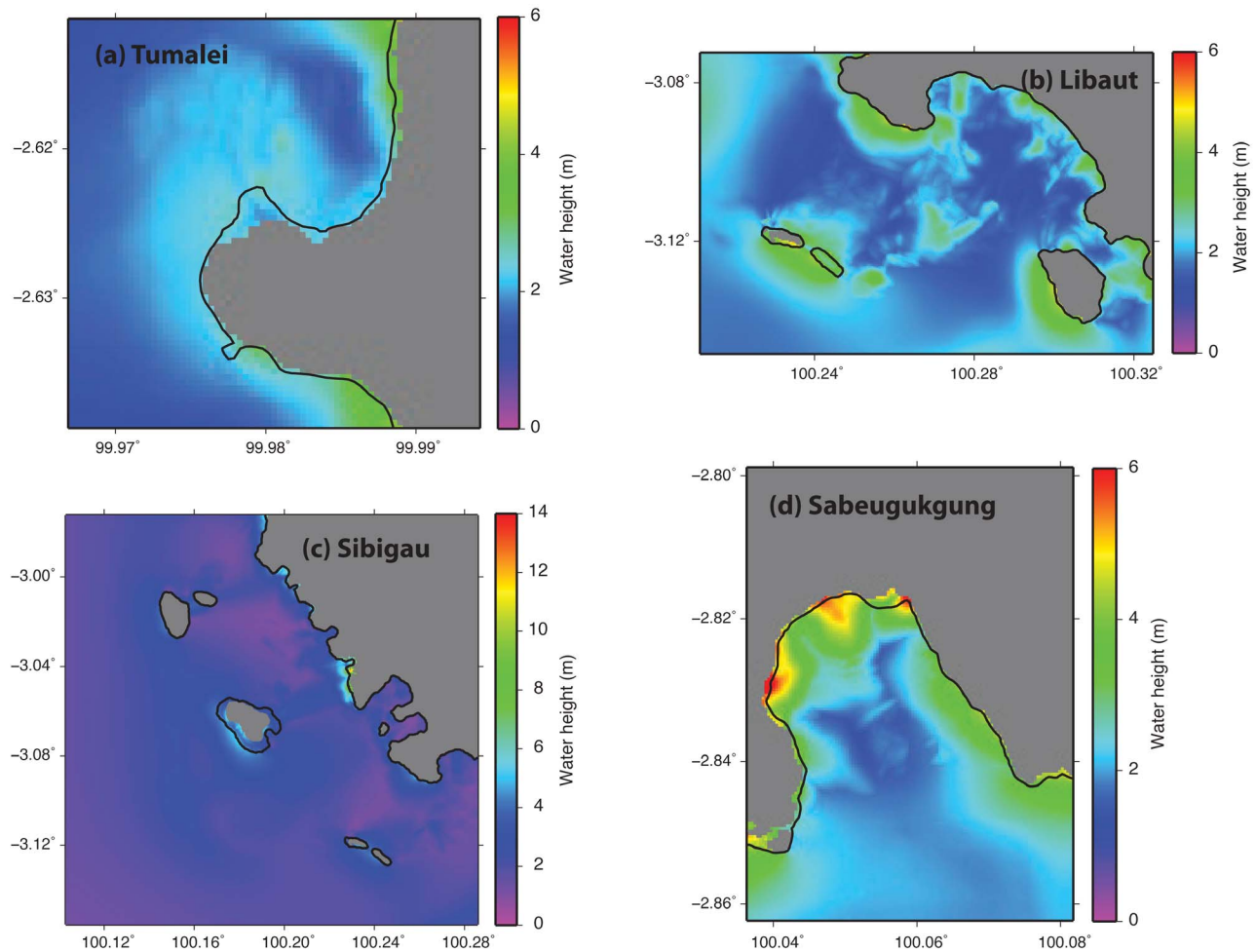


**Figure 20.** Tsunami inundation and water height for various survey locations (Figure 3). The tsunami model was initiated using the source model shown in Figure 15 (not including additional inelastic sediment uplift).

between the line of highest slip and the trench burial point (uplift grids used to initiate the tsunami modeling, with and without this effect included, are illustrated in Figures S8 and S9 in Text S1 of the auxiliary material). This gives a combined elastic and inelastic uplift of  $>4$  m over the area of highest slip, and accounts for more than half of the tsunami effect in the resulting model. This gives improved agreement between the tsunami model and measurements (Figure 17). The weighted mean of the sum of squared residuals (assuming uncertainties of 1 m) for the tsunami models are 7 and 13, with and without this additional uplift, respectively. Since we have reasons to expect that the tsunami modeling will result in an underprediction of the runup (as discussed above), it is likely that our ad-hoc uplift model is too large, but these results suggest that this process could be important to consider. The agreement of the model to the DART record (Figure 18) is considerably improved when the additional uplift is included.

[52] Figure 19 shows comparisons of survey and model results, with and without the sediment effect included, for several sub-regions of the affected area. Results in these figures marked as “nearest location” indicate those for which the numerical prediction is for the numerical grid point

closest to the survey location. Results marked as “exact location” were obtained by linear interpretation of simulated runup heights. Figures 20 and 21 show model inundation maps for various survey locations, with and without the sediment effect included. The inundation maps highlight the difference in simulated runup resulting from including the additional inelastic uplift.

## 8. Discussion

[53] One of our most important results is that the relatively small GPS displacements preclude megathrust slip near the islands from contributing significantly to the tsunami; regardless of the a priori slip parameters, inversions are unable to place the primary rupture patch more than  $\sim 50$  km from the trench or at depths  $>6$  km. Although we are unable to resolve complexities in the slip distribution, and large uncertainties on the amount of slip remain, the conclusion that the majority of slip occurred far from the islands at very shallow depths is robust. Our results also imply that inelastic deformation of trench sediments could be an important component of tsunami earthquakes. We cannot rule out a contribution to this tsunami from splay faulting and/or a

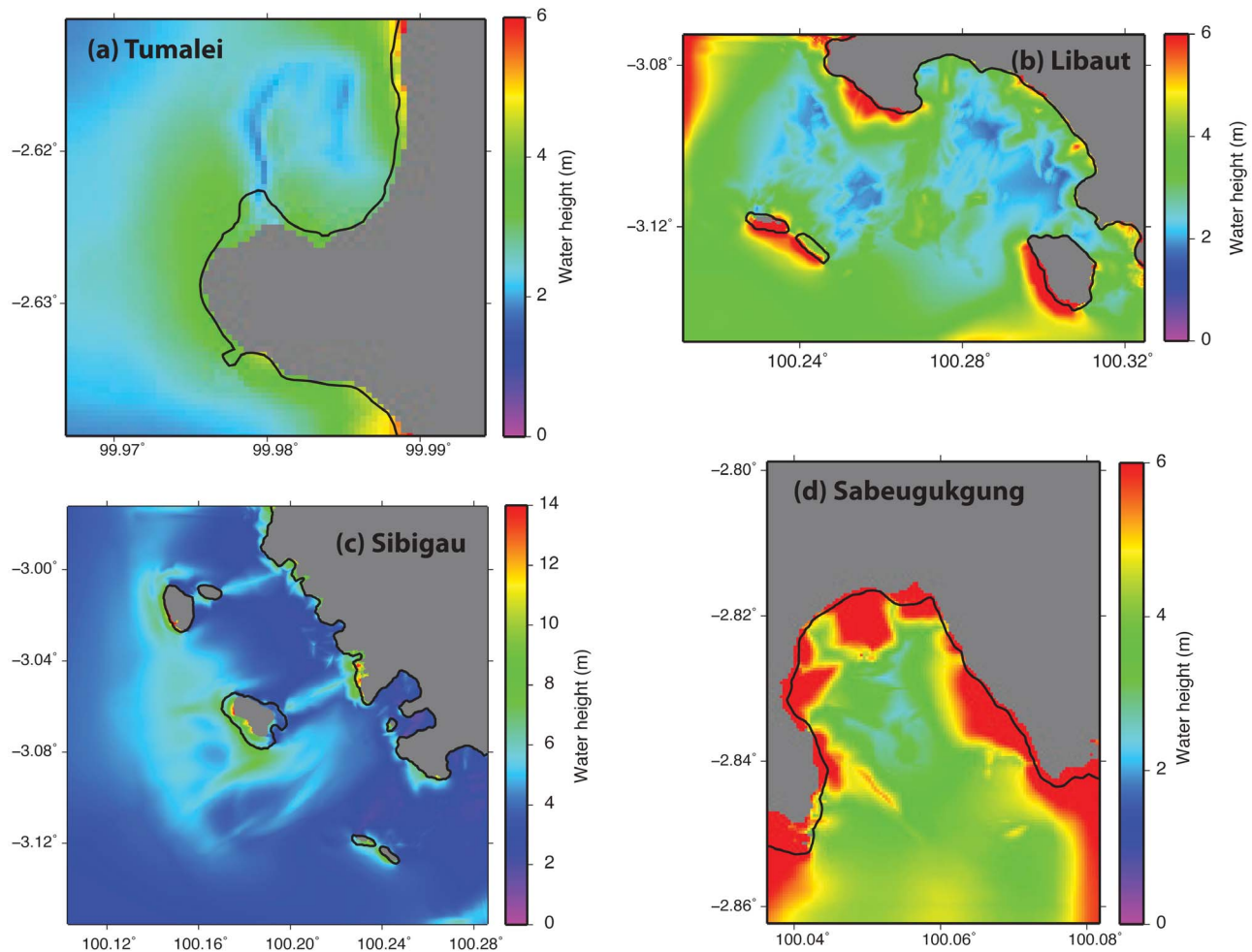


**Figure 21.** Same as Figure 20, but the tsunami model was initiated using a source model that included inelastic sediment uplift in addition to elastic effects. For Sabeugukgung the color bar saturates at the upper limit.

seafloor landslide, but the seismic profiles of *Singh et al.* [2011] suggest to us that inelastic deformation may be a more likely contributor. The large spatial extent of the tsunami (runup >5 m over ~100 km of the Mentawai coast) indicates that a landslide was unlikely to be the primary cause, since landslides usually cause more localized tsunamis. For example, the 1998 Papua New Guinea tsunami was determined to have been caused by a submarine slump in conjunction with an earthquake of  $M_S$  7.0 [Synolakis et al., 2002], but extreme tsunami effects were only observed over ~30 km of the coastline.

[54] The October 2010 megathrust rupture occurred far updip of the megathrust rupture that generated the September 2007  $M_w$  8.4 earthquake and tsunami [Konca et al., 2008; Borrero et al., 2009] (Figure 1). However, just as the 2007 earthquake and its immediate aftershocks, the 2010 event occurred on the Mentawai patch [Sieh et al., 2008], which has not fully ruptured since the great events of 1833 ( $M \sim 9$ ) and 1797 ( $M \sim 8.8$ ) [Natawidjaja et al., 2006]. Since the combination of moment relieved during the 2007 and 2010 ruptures is far short of all the strain accumulated in the region of the Mentawai patch since these historic earthquakes, the

forecast of *Sieh et al.* [2008] of a large future earthquake and associated tsunami [Borrero et al., 2006] remains unrealized.

[55] Another important observation is that the 2010 earthquake rupture includes an area of the megathrust that had previously been designated as weakly coupled [Chlieh et al., 2008], that is a portion of the fault plane along which slip is accommodated by stable sliding and therefore embodying a low or nil seismic hazard. This shallow area of subduction zones is commonly assumed to have weak coupling, due to the presence of unconsolidated sediments, observations that seismicity does not generally extend all the way to the trench [Byrne et al., 1988], and the hypothesis that the updip limit of the seismogenic zone may be controlled by stable-sliding clays [Vrolijk, 1990]. Not only do our results show that this shallow area can rupture with devastating consequences, in the form of a large tsunami, but by increasing the potential width that can be ruptured in great earthquakes we could infer larger earthquakes here than previously forecast. This work indicates that in earthquake and tsunami scenario planning we should rethink this of shallow aseismicity. Similarly, our results, along with the checkerboard resolution tests of *Chlieh et al.* [2008], indicate that the designation of low

coupling along the shallowest portions of the megathrust was not strongly defensible, due to the significant distance from the geodetic observations. Seafloor geodetic measurements are needed to improve our understanding of strain accumulation and relief along this very shallow portion of the fault. The March 2011 Tohoku-Oki earthquake has raised similar questions, since this also saw high levels of slip on shallow areas of the megathrust that had previously been thought to be aseismic [Avouac, 2011]. Our work is significant in that unlike studies of this very large earthquake, we are able to put tight constraints on quite how shallow a rupture is possible.

[56] Based on the small vertical displacements of the islands during this earthquake, these results indicate that paleogeodetic records of past earthquakes [Natawidjaja *et al.*, 2006] would not detect an earthquake of this type. However, there are indications that at least one other similar earthquake has occurred on this subduction zone; Kanamori *et al.* [2010] examined historical seismograms to conclude that the  $M \sim 7.6$  1907 Sumatra earthquake also had all the attributes of a tsunami earthquake, and also ruptured a narrow patch close to the trench. The societal memory of this earthquake and its extensive tsunami was the reason that many residents of Simeulue Island knew to evacuate to higher ground immediately after the 2004 Aceh-Andaman earthquake [McAdoo *et al.*, 2006].

[57] Published slip distributions for both the 2007  $M_w$  8.4 [Konca *et al.*, 2008] and the 2005  $M_w$  8.6 Nias-Simeulue [Briggs *et al.*, 2006] earthquake to the north, do not suggest that these events ruptured all the way to the trench. However, checkerboard resolution tests made as part of these studies indicate that firm conclusions on shallow slip were not possible. It has been suggested from seismic survey evidence [Singh *et al.*, 2008] that the 2004 Sumatra-Andaman  $M_w$  9.15 earthquake [Chlieh *et al.*, 2007] did propagate all the way to the surface.

[58] This therefore raises the important question of whether other shallow segments of the Sunda megathrust could still fail, potentially causing equally catastrophic tsunami. Can only certain areas of the shallow fault accommodate large earthquakes, with variations in coupling perhaps due to the presence of bathymetric features from horst and graben structures or seamounts [Polet and Kanamori, 2000; Tanioka *et al.*, 1997; Wang and Bilek, 2011]? Is the seismic behavior of this shallow region transient, perhaps influenced by the presence of fluids released by subducted sediments [Bilek and Lay, 1998; Seno, 2002], or can the shallow areas be locked over long periods of time? And can strain loading from previous large earthquakes, in this case the 2007 earthquake and its afterslip, result in bimodal behavior of conditionally stable zones [Bilek and Lay, 2002]? Our results indicate that further investigation of these questions, perhaps through a combination of geophysical survey and seafloor geodetic techniques, is of critical importance to the safety of people living on the doorstep of this and other subduction zones.

## Appendix A: Lessons Learned for Outreach Efforts

[59] This event illustrated areas for improvement in terms of tsunami education and awareness campaigns directed at the local population as well as in planning for tsunami evacuations. In the first case, while most residents were well

aware of tsunamis being associated with earthquakes, there was a notion, based on educational material, that the potential threat of a tsunami was related to the strength of the ground shaking during the earthquake. This perception was skewed by the fact that the 2007 Bengkulu earthquake caused significant ground shaking and coseismic uplift but did not cause a damaging tsunami in the Mentawai Islands and only a moderate tsunami on the coast of Mainland Sumatra [Borrero *et al.*, 2009]. Thus, with the relatively gentle and slow ground shaking, many residents assumed that there would not be a tsunami and did not evacuate. It was not until they heard the sound of the approaching wave that residents were prompted into action, but by then it was too late.

[60] Related to the second point, it was clear that proximity and access to high ground was directly related to survivability of the tsunami in the villages that we visited. Particularly striking was the comparison between Sabeugukung and Tumalei villages. Both sites experienced roughly equal tsunami effects and both villages had some level of awareness of tsunami hazards. However, in the case of Sabeugukung, the village was located on a peninsula at the back of a bay with the ocean on one side and a brackish stream on the other. When it came time to evacuate, the shortest route to high ground was across the stream and residents were not able to get across before the tsunami struck. As a result, the majority of the villagers were killed by the tsunami. At Tumalei, the village was situated on a narrow coastal plain at the foot of a steep hill. Despite not evacuating immediately after the earthquake, when it was clear that the tsunami was approaching the residents were able to quickly get to high ground and there were not casualties, despite the fact that the entire village was destroyed. Additionally, guests at the 'Macaronis' resort escaped the tsunami by going up to the third floor of the resort compound. The tsunami surge inundated over the first floor and did serious damage to the structure, but withstood the tsunami and remained standing.

[61] These examples suggest that messages contained in tsunami education and outreach material should be modified to include the duration of the ground shaking as a trigger for spontaneous evacuations. Furthermore, these cases show that evacuation planning, defining and establishing evacuation routes and practice drills can result in fewer casualties.

[62] **Acknowledgments.** This work was funded by the Earth Observatory of Singapore (EOS) and is EOS Contribution Number 37. The tsunami helicopter survey was partially supported by NSF RAPID CMMI-1105577. E.H. is partially supported by a Singapore National Research Foundation fellowship. We are grateful to Lujia Feng, Ashar Lubis, Judith Hubbard, and Brad Aagaard for useful discussions and to Jeffrey Encillo for logistical and technical support. We also thank reviewers Andreas Hoechner, Ya-Ju Hsu, and the Associate Editor for their insightful comments and suggestions. We acknowledge Captain Lee Clark of the vessel MV *Freedom III* for his vivid account of the tsunami at Macaroni Bay.

## References

- Altamimi, Z., X. Collilieux, J. Legrand, B. Garayt, and C. Boucher (2007), ITRF2005: A new release of the International Terrestrial Reference Frame based on time series of station positions and Earth Orientation Parameters, *J. Geophys. Res.*, *112*, B09401, doi:10.1029/2007JB004949.
- Avouac, J.-P. (2011), The lessons of Tohoku-Oki, *Nature*, *475*, 300, doi:10.1038/nature10265.
- Barnhart, W. D., and R. B. Lohman (2010), Automated fault model discretization for inversions for coseismic slip distributions, *J. Geophys. Res.*, *115*, B10419, doi:10.1029/2010JB007545.

- Bertiger, W., S. D. Desai, B. Haines, N. Harvey, A. W. Moore, S. Owen, and J. P. Weiss (2010), Single receiver phase ambiguity resolution with GPS data, *J. Geod.*, *84*, 327–337, doi:10.1007/s00190-010-0371-9.
- Bilek, S. L., and T. Lay (1998), Variation of interplate fault zone properties with depth in the Japan subduction zone, *Science*, *281*, 1175–1178.
- Bilek, S. L., and T. Lay (2002), Tsunami earthquakes possibly widespread manifestations of frictional conditional stability, *Geophys. Res. Lett.*, *29*(14), 1673, doi:10.1029/2002GL015215.
- Bird, P. (2003), An updated digital model of plate boundaries, *Geochem. Geophys. Geosyst.*, *4*(3), 1027, doi:10.1029/2001GC000252.
- Blewitt, G. (1989), Carrier phase ambiguity resolution for the Global Positioning System applied to geodetic baselines up to 2000 km, *J. Geophys. Res.*, *94*(B8), 10,187–10,203.
- Borrero, J. C., K. Sieh, M. Chlieh, and C. E. Synolakis (2006), Tsunami inundation modeling for western Sumatra, *Proc. Natl. Acad. Sci. U. S. A.*, *103*(52), 19,673–19,677.
- Borrero, J. C., R. Weiss, E. A. Okal, R. Hidayat, S. D. Arcas, and V. V. Titov (2009), The tsunami of september 12, 2007, Bengkulu Province, Sumatra, Indonesia: Post-tsunami field survey and numerical modeling, *Geophys. J. Int.*, *178*, 180–194, doi:10.1111/j.1365-246X.2008.04058.x.
- Briggs, R. W., et al. (2006), Deformation and slip along the Sunda megathrust in the great 2005 Nias-Simeulue earthquake, *Science*, *311*, 1897–1901.
- Byrne, D. E., D. M. Davis, and L. R. Sykes (1988), Loci and maximum size of thrust earthquakes and the mechanics of the shallow region of subduction zones, *Tectonics*, *7*(4), 833–857.
- Chlieh, M., et al. (2007), Coseismic slip and afterslip of the great Mw 9.15 Sumatra-Andaman earthquake of 2004, *Bull. Seismol. Soc. Am.*, *97*(1A), S152–S173, doi:10.1785/0120050631.
- Chlieh, M., J.-P. Avouac, K. Sieh, D. H. Natawidjaja, and J. Galetzka (2008), Heterogeneous coupling of the Sumatran megathrust constrained by geodetic and paleogeodetic measurements, *J. Geophys. Res.*, *113*, B05305, doi:10.1029/2007JB004981.
- Choi, K., A. Bilich, K. M. Larson, and P. Axelrad (2004), Modified sidereal filtering: Implications for high-rate GPS positioning, *Geophys. Res. Lett.*, *31*, L22608, doi:10.1029/2004GL021621.
- Cummins, P. R., and Y. Kaneda (2000), Possible splay fault slip during the 1946 Nankai earthquake, *Geophys. Res. Lett.*, *27*(17), 2725–2728.
- Du, Y., A. Aydin, and P. Segall (1992), Comparison of various inversion techniques as applied to the determination of a geophysical deformation model for the 1983 Borah Peak earthquake, *Bull. Seismol. Soc. Am.*, *82*(4), 1840–1866.
- Elosegui, P., J. L. Davis, J. M. Johansson, and I. I. Shapiro (1996), Detection of transient motions with the Global Positioning System, *J. Geophys. Res.*, *101*(B5), 11,249–11,261.
- Fritz, H. M., et al. (2007), Extreme runup from the 17 July 2006 Java tsunami, *Geophys. Res. Lett.*, *34*, L12602, doi:10.1029/2007GL029404.
- Harris, R. A., and P. Segall (1987), Detection of a locked zone at depth on the Parkfield, California, segment of the San Andreas fault, *J. Geophys. Res.*, *92*(B8), 7945–7962.
- Hayakawa, Y. S., T. Oguchi, and Z. Lin (2008), Comparison of new and existing global digital elevation models: ASTER G-DEM and SRTM-3, *Geophys. Res. Lett.*, *35*, L17404, doi:10.1029/2008GL035036.
- Herring, T. A., R. W. King, and S. C. McClusky (2005), GLOBK, Global Kalman filter VLBI and GPS analysis program, report, Mass. Inst. of Technol., Cambridge.
- Hsu, Y.-J., M. Simons, J.-P. Avouac, J. Galetzka, K. Sieh, M. Chlieh, D. Natawidjaja, L. Prawirodirdjo, and Y. Bock (2006), Frictional afterslip following the 2005 Nias-Simeulue earthquake, Sumatra, *Science*, *312*, 1921–1926.
- Hsu, Y.-J., M. Simons, C. Williams, and E. Casarotti (2011), Three-dimensional FEM derived elastic Green's functions for the coseismic deformation of the 2005 Mw 8.7 Nias-Simeulue, Sumatra earthquake, *Geochem. Geophys. Geosyst.*, *12*, Q07013, doi:10.1029/2011GC003553.
- Kanamori, H. (1972), Mechanism of tsunami earthquakes, *Phys. Earth Planet. Inter.*, *6*, 346–359.
- Kanamori, H., L. Rivera, and W. H. K. Lee (2010), Historical seismograms for unraveling a mysterious earthquake: The 1907 Sumatra earthquake, *Geophys. J. Int.*, *183*, 358–374, doi:10.1111/j.1365-246X.2010.04731.x.
- Kanoglu, U., and C. E. Synolakis (1998), Long wave runup on piecewise linear topographies, *J. Fluid Mech.*, *374*, 1–28.
- King, R., and Y. Bock (2005), Documentation for the GAMIT GPS analysis software, report, Mass. Inst. of Technol., Cambridge.
- Konca, A. O., et al. (2008), Partial rupture of a locked patch of the Sumatra megathrust during the 2007 earthquake sequence, *Nature*, *456*, 631–635, doi:10.1038/nature07572.
- Lawson, C. L., and R. J. Hanson (1974), *Solving least squares problems*, Prentice-Hall, Englewood Cliffs, N. J.
- Lay, T., and S. Bilek (2007), Anomalous earthquake ruptures at shallow depths on subduction zone megathrusts, in *The Seismogenic Zone of Subduction Thrust Faults*, edited by T. H. Dixon and J. C. Moore, pp. 476–511, Columbia Univ. Press, New York.
- Lay, T., C. J. Ammon, H. Kanamori, Y. Yamazaki, K. F. Cheung, and A. R. Hutko (2011), The 25 October 2010 Mentawai tsunami earthquake (Mw 7.8) and the tsunami hazard presented by shallow megathrust ruptures, *Geophys. Res. Lett.*, *38*, L06302, doi:10.1029/2010GL046552.
- Liu, P. L. F., Y. S. Cho, S. B. Yoon, and S. N. Seo (1994), Numerical simulations of the 1960 Chilean tsunami propagation and inundation at Hilo, Hawaii, in *Recent Developments in Tsunami Research*, edited by M. I. El-Sabh, pp. 99–115, Kluwer Acad., Dordrecht, Netherlands.
- McAdoo, B. G., L. Dengler, G. Prasetya, and V. Titov (2006), How an oral history saved thousands on Indonesia's Simeulue island during the December 2004 and March 2005 tsunamis, *Earthquake Spectra*, *22*(S3), 661–669, doi:10.1193/1.2204966.
- Meltzner, A. J., K. Sieh, H.-W. Chiang, C.-C. Shen, B. W. Suwargadi, D. H. Natawidjaja, B. E. Philibosian, R. W. Briggs, and J. Galetzka (2010), Coral evidence for earthquake recurrence and an A.D. 1390–1455 cluster at the south end of the 2004 Aceh–Andaman rupture, *J. Geophys. Res.*, *115*, B10402, doi:10.1029/2010JB007499.
- Menke, W. (1989), *Geophysical Data Analysis: Discrete Inverse Theory*, Academic, San Diego, Calif.
- Moore, G. F., N. L. Bangs, A. Taira, S. Kuramoto, E. Pangborn, and H. J. Tobin (2007), Three-dimensional splay fault geometry and implications for tsunami generation, *Science*, *318*, 1128–1131.
- Natawidjaja, D. H., K. Sieh, M. Chlieh, J. Galetzka, B. W. Suwargadi, H. Cheng, R. L. Edwards, J.-P. Avouac, and S. N. Ward (2006), Source parameters of the great Sumatran megathrust earthquakes of 1797 and 1833 inferred from coral microatolls, *J. Geophys. Res.*, *111*, B06403, doi:10.1029/2005JB004025.
- Newman, A. V., G. Hayes, Y. Wei, and J. Convers (2011), The 25 October 2010 Mentawai tsunami earthquake, from real-time discriminants, finite-fault rupture, and tsunami excitation, *Geophys. Res. Lett.*, *38*, L05302, doi:10.1029/2010GL046498.
- Okada, Y. (1985), Surface deformation due to shear and tensile faults in a half-space, *Bull. Seismol. Soc. Am.*, *75*(4), 1135–1154.
- Okal, E. A., and A. V. Newman (2001), Tsunami earthquakes: The quest for a regional signal, *Phys. Earth Planet. Inter.*, *124*, 45–70.
- Page, M. T., S. Custodio, R. J. Archuleta, and J. M. Carlson (2009), Constraining earthquake source inversions with GPS data: 1. Resolution-based removal of artifacts, *J. Geophys. Res.*, *114*, B01314, doi:10.1029/2007JB005449.
- Polet, J., and H. Kanamori (2000), Shallow subduction zone earthquakes and their tsunamigenic potential, *Geophys. J. Int.*, *142*, 684–702.
- Seno, T. (2000), The 21 September, 1999 Chi-Chi earthquake in Taiwan: Implications for tsunami earthquakes, *Terr. Atmos. Ocean Sci.*, *11*(3), 701–708.
- Seno, T. (2002), Tsunami earthquake as transient phenomena, *Geophys. Res. Lett.*, *29*(10), 1419, doi:10.1029/2002GL014868.
- Sieh, K., et al. (2008), Earthquake supercycles inferred from sea-level changes recorded in the corals of west Sumatra, *Science*, *322*, 1674–1678.
- Singh, S. C., et al. (2008), Seismic evidence for broken oceanic crust in the 2004 Sumatra earthquake epicentral region, *Nat. Geosci.*, *1*, 777–781.
- Singh, S. C., N. Hananto, M. Mukti, H. Permana, Y. Djajadihardja, and H. Harjono (2011), Seismic images of the megathrust rupture during the 25th October 2010 Pagai earthquake, SW Sumatra: Frontal rupture and large tsunami, *Geophys. Res. Lett.*, *38*, L16313, doi:10.1029/2011GL048935.
- Smith, B., and D. Sandwell (2003), Accuracy and resolution of shuttle radar topography mission data, *Geophys. Res. Lett.*, *30*(9), 1467, doi:10.1029/2002GL016643.
- Stefanakis, T. S., F. Dias, and D. Dutykh (2011), Local run-up amplification by resonant wave interactions, *Phys. Rev. Lett.*, *107*, 124502, doi:10.1103/PhysRevLett.107.124502.
- Synolakis, C. E., J.-P. Bardet, J. C. Borrero, H. L. Davies, E. A. Okal, E. A. Silver, S. Sweet, and D. R. Tappin (2002), The slump origin of the 1998 Papua New Guinea tsunami, *Proc. R. Soc. A*, *458*, 763–789.
- Tanioka, Y., and T. Seno (2001), Sediment effect on tsunami generation of the 1896 Sanriku tsunami earthquake, *Geophys. Res. Lett.*, *28*(17), 3389–3392.
- Tanioka, Y., L. Ruff, and K. Satake (1997), What controls the lateral variation of large earthquake occurrence along the Japan trench?, *Isl. Arc*, *6*, 261–266.
- Van Niel, T. G., T. R. McVicar, L. Li, J. C. Gallant, and Q. Yang (2008), The impact of misregistration on SRTM and DEM image differences, *Remote Sens. Environ.*, *112*, 2430–2442.

- Vrolijk, P. (1990), On the mechanical role of smectite in subduction zones, *Geology*, *18*, 703–707.
- Wang, K., and S. L. Bilek (2011), Do subducting seamounts generate or stop large earthquakes?, *Geology*, *39*(9), 819–822, doi:10.1130/G31856.1.
- Wang, R., F. L. Martin, and F. Roth (2003), Computation of deformation induced by earthquakes in a multi-layered elastic crust: FORTRAN programs EDGRN/EDCMP, *Comput. Geosci.*, *29*, 195–207.
- Wendt, J., D. D. Oglesby, and E. L. Geist (2009), Tsunamis and splay fault dynamics, *Geophys. Res. Lett.*, *36*, L15303, doi:10.1029/2009GL038295.
- Zumberge, J. F., M. B. Heflin, D. C. Jefferson, M. M. Watkins, and F. H. Webb (1997), Precise point positioning for the efficient and robust analysis of GPS data from large networks, *J. Geophys. Res.*, *102*, 5005–5018.